Rho GTPase signaling and mDia facilitate endocytosis via presynaptic actin

Kristine Oevel[1], Svea Hohensee[1], Atul Kumar[2], Irving Rosas-Brugada[1#], Francesca Bartolini[2], Tolga Soykan[1*], and Volker Haucke[1,3,4*]

[1] Leibniz-Forschungsinstitut für Molekulare Pharmakologie (FMP), 13125 Berlin, Germany.

[2] Department of Pathology and Cell Biology, Columbia University Medical Center, New York, NY 10032, USA.

[3] Faculty of Biology, Chemistry, Pharmacy, Freie Universität Berlin, 14195 Berlin, Germany.

[4] NeuroCure Cluster of Excellence, Charité Universitätsmedizin Berlin, 10117 Berlin, Germany.

*Correspondence: haucke@fmp-berlin.de (V.H.) or soykan@fmp-berlin.de (T.S.).

[#] deceased

ABSTRACT

Neurotransmission at synapses is mediated by the fusion and subsequent endocytosis of synaptic vesicle membranes. Actin has been suggested to be required for presynaptic endocytosis but the mechanisms that control actin polymerization and its mode of action within presynaptic nerve terminals remain poorly understood. We combine optical recordings of presynaptic membrane dynamics and ultrastructural analysis with genetic and pharmacological manipulations to demonstrate that presynaptic endocytosis is controlled by actin regulatory diaphanous-related formins mDia1/3 and Rho family GTPase signaling. We show that impaired presynaptic actin assembly in the near absence of mDia1/3 and reduced RhoA activity is partly compensated by hyperactivation of Rac1. Inhibition of Rac1 signaling further aggravates impaired presynaptic endocytosis elicited by loss of mDia1/3. Our data suggest that interdependent mDia1/3-Rho and Rac1 signaling pathways cooperatively act to facilitate synaptic vesicle endocytosis by controlling presynaptic F-actin.

INTRODUCTION

Synaptic transmission relies on the release of neurotransmitters by calcium-triggered exocytic fusion of synaptic vesicles (SVs) at specialized active zone release sites within presynaptic nerve terminals. Following fusion, compensatory endocytosis retrieves SV proteins and lipids from the presynaptic plasma membrane and SVs are reformed (Chanaday *et al*, 2019; Gan & Watanabe, 2018; Kononenko & Haucke, 2015; Saheki & De Camilli, 2012; Soykan *et al*, 2016), e.g. by clathrin-mediated vesicle budding (Kononenko *et al*, 2014; Watanabe *et al*, 2014) (but see (Wu *et al*, 2014) for evidence in favor of clathrin-independent SV reformation). Endocytosis relies on mechanical forces to enable membrane deformation and eventually fission (Engqvist-Goldstein & Drubin, 2003). In many biological systems, actin and actin-associated myosin motors appear to provide such mechanical force to facilitate vesicle formation (Anes *et al*, 2003; Marston *et al*, 2003). For example, the function of actin for endocytosis is well-established in yeast, whereas differential requirements for actin in distinct forms of endocytosis have been described in various types of mammalian cells including neurons (Boulant *et al*, 2011; Merrifield *et al*, 2005; Saffarian *et al*, 2009; Saheki & De Camilli, 2012). Pharmacological inhibition of actin assembly by latrunculin has been shown to cause the accumulation of endocytic intermediates at lamprey giant synapses (Shupliakov *et al*, 2002) and interfere with ultrafast endocytosis in response to single optical action potentials (APs) at hippocampal synapses (Watanabe *et al*, 2013; Watanabe *et al.*, 2014; Wu & Chan, 2022) and with fast endocytosis at cerebellar mossy fiber boutons (Delvendahl *et al*, 2016). The same treatment does not hamper endocytosis of SV proteins at hippocampal synapses stimulated with trains of APs (Sankaranarayanan *et al*, 2003; Soykan *et al*, 2017). Genetic interference with actin function by conditional knockout (KO) of β- or γ-actin genes has suggested a crucial role for actin in all kinetically distinguishable forms of endocytosis (Wu *et al*, 2016) at hippocampal synapses and the calyx of Held, a fast giant synapse in the auditory

53 brain stem (Borst & Soria van Hoeve, 2012). However, in the same preparations actin loss also
54 affected SV exocytosis (Wu *et al.*, 2016), suggesting a more general requirement of actin for
55 presynaptic function. Consistently, actin has been shown to surround clusters of reserve pool SVs
56 in lamprey (Bloom *et al*, 2003), to facilitate the replenishment of fast releasing vesicles in various
57 models (Sakaba *et al*, 2013; Sakaba & Neher, 2003), to be involved in Tau pathology (Zhou *et al*,
58 2017), to induce spine growth and plasticity, (Cingolani & Goda, 2008) and to steer neuronal
59 migration (Shinohara *et al*, 2012) among various other roles.

60 We have previously demonstrated that pharmacological interference with the function of
61 formins, a group of Rho family-associated proteins that nucleate linear filamentous (F) actin,
62 kinetically delays SV endocytosis at hippocampal boutons and blocks compensatory endocytosis
63 at the calyx of Held in pre-hearing rats (Soykan *et al.*, 2017). Capacitance measurements at the
64 calyx of Held in post-hearing rodents suggest a less stringent requirement for formin-mediated
65 actin assembly for endocytosis (Hori *et al*, 2022). The latter observation may reflect the operation
66 of compensatory pathways for actin assembly, e.g. via Rac1 or Cdc42 Rho-family GTPases that
67 promote branched actin networks (Eisenmann *et al*, 2005; Goode & Eck, 2007; Hodge & Ridley,
68 2016).

69 In contrast to the vast body of literature regarding the role of actin and actin-associated
70 proteins at the postsynapse [(Cingolani & Goda, 2008; Colgan & Yasuda, 2014) and references
71 therein], most notably the actin-rich mesh of the postsynaptic density of glutamatergic synapses,
72 comparably little is known about the signaling pathways (e.g. via guanine nucleotide exchange
73 factors and GTPase activating proteins for Rho family small GTPases (Muller *et al*, 2020)) that
74 mediate actin assembly at the presynapse. Recent work has suggested that presynaptic Rac1
75 negatively regulates synaptic strength and release probability by altering SV priming and
76 replenishment at central synapses (O'Neil *et al*, 2021) including the calyx of Held (Keine *et al*,

77 2022). These data suggest a negative regulatory role for Rac1 in SV exocytosis. The abundance of
78 postsynaptic actin (Chen *et al*, 2020; Cingolani & Goda, 2008; Colgan & Yasuda, 2014) has
79 hampered the analysis of the nanoscale localization of actin at presynaptic nerve terminals and of
80 the actin-regulatory proteins that control its dynamics. KO of Dynamin, the main enzyme for
81 endocytic membrane fission (Ferguson *et al*, 2007; Imoto *et al*, 2022; Raimondi *et al*, 2011), has
82 been shown to cause the accumulation of F-actin at and around stalled endocytic intermediates in
83 non-neuronal cells (Ferguson *et al*, 2009) but this phenotype seems less overt at hippocampal
84 synapses (Raimondi *et al.*, 2011). Hence, actin in addition to a possible local role at endocytic
85 invaginations might serve a more general function in endocytosis at synapses, for example by
86 modulating plasma membrane tension or contractility, by providing a restrictive membrane
87 scaffold that promotes membrane fission by keeping endocytic invaginations under longitudinal
88 tension (Boulant *et al.*, 2011; Roux *et al*, 2006; Wu & Chan, 2022), or via formation of an F-actin
89 ring around the active zone that mechanically couples exocytic membrane compression to
90 endocytic pit formation (Ogunmowo *et al*, 2023).
91 Here we combine optical recordings of SV exo-/ endocytosis and ultrastructural analysis
92 with genetic and pharmacological manipulations to show that interdependent mDia1/3-Rho and
93 Rac1 signaling pathways cooperate to facilitate SV endocytosis by controlling presynaptic F-actin.
94

95 **RESULTS**

96 *Actin dynamics and actin nucleating mDia1/3 proteins facilitate presynaptic endocytosis and SV*
97 *recycling*

98 Previous studies using pharmacological inhibitors of actin polymerization and
99 depolymerization have yielded inconclusive, often conflicting data regarding the function of actin
100 in SV endocytosis and recycling in different models (Bleckert *et al*, 2012; Del Signore *et al*, 2021;

101 Piriya Ananda Babu *et al*, 2020; Sankaranarayanan *et al.*, 2003; Shupliakov *et al.*, 2002; Wu &
102 Chan, 2022). In contrast, genetic ablation of β- or γ-actin genes in mouse neurons suggests that
103 actin is required for all forms of endocytosis at several types of synapses (Wu *et al.*, 2016).
104 Prompted by these findings we revisited the role of actin in presynaptic endocytosis by analyzing
105 the effects of impaired F-actin dynamics in the combined presence of the G-actin sequestering
106 drug latrunculin A, the F-actin stabilizer jasplakinolide, and Y-27632, an inhibitor of ROCK kinase
107 signaling. This cocktail was shown to preserve the existing cytoskeleton architechture while
108 blocking actin assembly, disassembly and rearrangement (Peng *et al*, 2011). We optically recorded
109 the stimulation-induced exo-endocytosis of the SV protein Synaptophysin (Syph) fused to a pH-
110 sensitive super-ecliptic green fluorescent protein (pHluorin) (Miesenbock *et al*, 1998) that is de-
111 quenched during exocytosis and undergoes re-quenching as SVs are internalized and re-acidified
112 in hippocampal neurons at physiological temperature. Under these conditions (i.e. trains of APs,
113 37°C), SV endocytosis occurs on a timescale of > 10 seconds, e.g. a timescale that is slower than
114 re-quenching of pHluorin due to reacidification (Lopez-Hernandez *et al*, 2022; Soykan *et al.*,
115 2017). Hence, the decay of pHluorin signals can serve as a measure of the time course of SV
116 endocytosis. Perturbation of actin dynamics in the combined presence of latrunculin A,
117 jasplakinolide, and Y-27632 significantly slowed down the endocytic retrieval of exogenously
118 expressed Syph-pHluorin (Figure 1A,B). As optical imaging of pHluorin reporters may lead to
119 artifacts, we analyzed the internalization kinetics of the endogenous vesicular γ-aminobutyric acid
120 transporter (vGAT) using antibodies directed against its luminal domain coupled to the pH-
121 sensitive fluorophore CypHer5E (Hua *et al*, 2011; Lopez-Hernandez *et al.*, 2022). The cyanine-
122 based dye CypHer5E is quenched at neutral pH but exhibits bright fluorescence when present in
123 the acidic lumen of SVs and, thus can serve as a tracer for the exo-endocytic cycling of endogenous
124 SV proteins. Perturbation of actin dynamics significantly delayed the endocytic retrieval of

125 endogenous vGAT in response to train stimulation with 200 APs at physiological temperature
126 (Figure 1C,D), consistent with the results from exogenously expressed Syph-pHluorin. Hence, a
127 dynamic actin cytoskeleton facilitates presynaptic endocytosis in hippocampal neurons.

128 Previous studies have suggested that formins, in particular mDia1, promote SV
129 endocytosis (Soykan *et al.*, 2017), likely by inducing F-actin assembly (Ganguly *et al*, 2015). We
130 confirmed that shRNA-mediated depletion of mDia1 from hippocampal neurons led to
131 significantly delayed Syph-pHluorin endocytosis and re-acidification in response to stimulation
132 with 200 APs. Re-expression of shRNA-resistant wild-type mDia1 fully restored normal
133 endocytosis kinetics (Figure 1E,F). Impaired SV endocytosis in lentivirus-mediated mDia1-
134 depleted neurons (Figure 1 Supplement 1A) was also observed, if SV exo-/ endocytosis was
135 triggered by stimulation with 40 APs or 80 APs and probed with vesicular glutamate transporter 1
136 (vGLUT1)-pHluorin (Figure 1G,H and Figure 1- Supplement 1B,C). Exocytic fusion of vGLUT1-
137 pHluorin-containing SVs was unaffected (Figure 1- Supplement 1D). Co-depletion of the closely
138 related mDia3 isoform tended to further aggravate this phenotype (Figure 1G,H and Figure 1-
139 Supplement 1B,C). Furthermore, mDia1/3 depletion significantly delayed the endocytic retrieval
140 of endogenous vGAT (Figure 1I,J). Conversely, application of IMM-01, a small molecule activator
141 of mDia-related formins that acts by relieving autoinhibition (Lash *et al*, 2013) (Figure 1-
142 Supplement 1E), led to a moderate but significant acceleration of SV endocytosis monitored by
143 vGLUT1-pHluorin (Figure 1K,L). Ultrastructural analysis of hippocampal synapses from
144 mDia1/3-depleted neurons by electron microscopy revealed a reduction in SV density compared
145 to controls (Figure 2A-C). This phenotype was rescued upon prior silencing of endogenous
146 neuronal network activity in the presence of tetrodotoxin (TTX) (Figure 2D and Figure 2-
147 Supplement 1A-E). A similar, slightly more pronounced depletion of SVs was observed in

148 hippocampal synapses from mDia1 knockout (KO) mice (Peng *et al*, 2007; Peng *et al*, 2003;
149 Shinohara *et al.*, 2012) (Figure 2E-G).
150 These data are consistent with a role for actin dynamics (see Fig. 1) and actin nucleating
151 mDia1/3 proteins in presynaptic endocytosis and SV recycling.
152
153 *mDia facilitates SV endocytosis by regulating presynaptic F-actin*
154 mDia1 in addition to its Rho binding domain and a C-terminal actin-assembling formin
155 homology 2 (FH2) domain comprises an unstructured N-terminal region involved in membrane
156 binding (Eisenmann *et al.*, 2005; Ramalingam *et al*, 2010) (Figure 3A). This architecture suggests
157 that mDia specifically promotes the nucleation of unbranched actin filaments at membranes, for
158 example to promote endocytosis at the presynaptic plasma membrane. To test this hypothesis, we
159 assayed the ability of mutant mDia1 lacking its N-terminal membrane-binding region (mDia1-ΔN)
160 (Ramalingam *et al.*, 2010) to rescue defective SV endocytosis in hippocampal neurons depleted of
161 endogenous mDia1. Mutant mDia1-ΔN displayed reduced association with membranes in
162 transfected HEK293T cells (Figure 3-Supplement 1A,B) and was unable to restore normal kinetics
163 of Syph-pHluorin endocytosis in hippocampal neurons transfected with mDia1-specific
164 microRNA (Figure 3B and Figure 3-Supplement 1C). Hence, mDia may act on SV endocytosis by
165 specifically promoting actin assembly at presynaptic membranes. We probed this model at several
166 levels. We analyzed the nanoscale localization and distribution of mDia1 via multicolor time-gated
167 stimulated emission depletion (gSTED) microscopy. Hippocampal neurons were stained for
168 mDia1, the presynaptic active zone marker Bassoon, and post-synaptic Homer 1. The distributions
169 of all three proteins along line profiles perpendicular to the synaptic cleft (i.e. the space between
170 Bassoon and Homer 1 clusters) were analyzed (Gerth *et al*, 2017). This analysis revealed that
171 endogenous mDia1 is primarily localized to the presynaptic compartment, where it is concentrated

172 at or very close to the plasma membrane (Figure 3D), i.e. < 50 nm away from the presynaptic
173 membrane (see (Dani *et al*, 2010)). Prompted by these results we dissected the interactome of
174 mDia1 by unbiased quantitative proteomic analyses of immunoprecipiates from detergent-
175 extracted mouse synaptosomes (Figure 3-Supplement 1D). In addition to actin, we identified a
176 variety of additional actin-regulatory proteins including Myosin IIB (Chandrasekar *et al*, 2013)
177 and the small GTPase Rac1 (Figure 3E). We confirmed the association of mDia1 with actin and
178 Myosin IIB (Figure 3-Supplement 1E) and found Myosin IIB to be concentrated at or near the
179 presynaptic plasma membrane (Figure 3-Supplement 1F,G) akin to the localization of mDia1. The
180 association of mDia1 with Myosin IIB is consistent with the inhibitory effects of the Myosin II
181 inhibitor blebbistatin on SV endocytosis (Chandrasekar *et al.*, 2013; Soykan *et al.*, 2017).
182 Interestingly, we also observed an enrichment of several endocytic proteins previously implicated
183 in SV recycling in mDia1 immunoprecipitates. These include the lipid phosphatase Synaptojanin1,
184 the bin-amphiphysin-rvs (BAR) domain proteins Amphiphysin, Endophilin A1, and PACSIN1/2
185 and, the GTPase Dynamin1 (Chanaday *et al.*, 2019; Gan & Watanabe, 2018; Saheki & De Camilli,
186 2012; Soykan *et al.*, 2016) (Figure 3E) as confirmed by immunoblotting (Figure 3F). Based on the
187 association of mDia1 with endocytic proteins including Dynamin1, we hypothesized that mDia1
188 might get stalled at endocytic intermediates that accumulate under conditions of perturbed
189 Dynamin function (Ferguson *et al.*, 2009; Raimondi *et al.*, 2011). Application of the partially non-
190 selective Dynamin inhibitor Dynasore (Macia *et al*, 2006) (Figure 3G,H) or expression of
191 dominant-negative mutant Dynamin1 K44A (Figure 3I-K) led to a significant accumulation of
192 mDia1 at presynaptic sites marked by Bassoon.

193 Based on these results we next investigated the relationship between mDia1/3 and
194 presynaptic actin. Multicolor gSTED imaging confirmed that F-actin labeled by phalloidin was
195 highly abundant at the postsynaptic compartment. In addition, F-actin was also visible, albeit at

196 reduced levels, in presynaptic boutons marked by Bassoon (Figure 4,B). Inhibition of Dynamin in
197 the presence of Dynasore (Figure 4C and Figure 4-Supplement 1A,B) or expression of Dynamin1
198 K44A (Figure 4-Supplement 1C-E) significantly elevated presynaptic F-actin levels within the
199 Bassoon area. These data are consistent with a role for presynaptic actin in SV endocytosis. We
200 directly tested the role of mDia in presynaptic actin nucleation and actin-dependent SV endocytosis
201 in several ways. First, we generated a mutant version of mDia1 that lacks the ability to nucleate
202 F-actin due to site-specific inactivation of its FH2 domain (Daou *et al*, 2014; Higashi *et al*, 2008;
203 Xu *et al*, 2004). We found that actin polymerization-defective mutant mDia1 (K994A) failed to
204 restore delayed vGLUT1-pHluorin endocytosis in mDia1-depleted hippocampal neurons (Figure
205 4D and Figure 4-Supplement 1F). Second, we analyzed the effects of depleting hippocampal
206 neurons of mDia1/3 on presynaptic F-actin. We found that loss of mDia1/3 significantly reduced
207 the amount of detectable F-actin within the Bassoon area (Figure 4A,E,F). To unequivocally
208 distinguish between presynaptic actin at exo-/ endocytic sites and the abundant pool of
209 postsynaptic actin associated with the postsynaptic density, we used the ORANGE strategy for
210 CRISPR-based genome-engineering (Willems *et al*, 2020) to generate eGFP-β-actin knock-in (KI)
211 hippocampal neurons. Due to the low knockin efficiency, this strategy allowed us to visualize
212 endogenously tagged eGFP-β-actin by 2-color gSTED imaging exclusively in presynaptic boutons
213 marked by vGLUT1. This assay confirmed the significant reduction in endogenous β-actin at
214 presynapses from mDia1/3-depleted neurons (Figure 4G-I). Third, we reasoned that if loss of
215 presynaptic actin in mDia-depleted neurons was causal for the observed defect in SV endocytosis,
216 pharmacological stabilization of F-actin might rescue the endocytic phenotype. Treatment of
217 mDia1/3-depleted neurons with jasplakinolide indeed fully restored the kinetics of SV endocytosis
218 monitored by vGLUT1-pHluorin (Fig. 4J and Figure 4-Supplement 1G,H).
219 We conclude that mDia1/3 facilitates SV endocytosis by regulating presynaptic F-actin.

220

221 *mDia1/3-Rho and Rac1 signaling pathways cooperatively act to facilitate presynaptic endocytosis*

222 In non-neuronal cells mDia proteins have been shown to be disinhibited by active Rho
223 family GTPases, in particular RhoA (Otomo *et al*, 2005) (Figure 5A and Figure 1 Supplement 1E).
224 We reasoned that Rho proteins might serve a similar function at presynaptic nerve terminals in
225 hippocampal neurons. Multicolor gSTED imaging revealed that endogenous RhoA was mostly
226 located within the presynaptic compartment (Figure 5B,C). Interference with Rho function by co-
227 expression of dominant-negative (DN) variants of RhoA and RhoB (Figure 5D and Figure 5-
228 Supplement 1A) or co-depletion of these Rho isoforms (Figure 5-Supplement 1B) delayed SV
229 endocytosis in response to stimulation with 200 APs. These results are consistent with a model in
230 which active Rho promotes mDia function and, thereby F-actin nucleation.

231 F-actin dynamics are known to be controlled by interdependent signaling networks
232 characterized by feedback regulation between components within the same pathway and between
233 key regulatory switches (e.g. distinct Rho/Rac family members) that drive distinct forms of F-actin
234 (see below) (Lawson & Ridley, 2018). For example, active mDia is known to stimulate RhoA
235 activation (Kitzing *et al*, 2007) (Figure 5A). Consistently, we found that RhoA activity was
236 reduced in hippocampal neurons depleted of mDia1/3 (Figure 5E,F). Work in non-neuronal cells
237 has further revealed that RhoA activity antagonizes activation of Rac1 (Chauhan *et al*, 2011), a
238 key factor for promoting the formation of branched F-actin networks at the cell cortex (Hodge &
239 Ridley, 2016; Lawson & Ridley, 2018) (Figure 6A). We hypothesized that reciprocally
240 interdependent Rho/ Rac1 signaling might control presynaptic F-actin assembly and, thereby, SV
241 endocytosis. In agreement with the alleged antagonistic regulation of RhoA and Rac1 function
242 (Lawson & Ridley, 2018), we found Rac1 activity to be significantly elevated in hippocampal
243 neurons depleted of mDia1/3 (Figure 6B,C), e.g. under conditions of reduced Rho-GTP levels. A

244 similar increase in active Rac1 levels was observed upon pharmacological inhibition of RhoA/B
245 in the presence of Rhosin (Figure 6-Supplement 1A). Multicolor gSTED imaging showed that
246 Rac1 was equally distributed between pre- and postsynaptic compartments in unperturbed
247 hippocampal neurons (Figure 6D,E). Elevated active Rac1 levels might conceivably ameliorate
248 presynaptic endocytic phenotypes elicted by mDia1/3 loss. In support of this hypothesis, we found
249 that selective pharmacological inhibition of Rac1 reduced presynaptic actin levels (Figure 6-
250 Supplement 1B-D) and caused a delay in the endocytic retrieval of endogenous vGAT (Figure
251 6F,G). Moreover, Rac1 inhibition further aggravated impaired vGAT endocytosis in mDia1/3-
252 depleted neurons. Expression of constitutively active GTP-locked Rac1 (Rac1-CA) restored
253 normal vGAT endocytosis kinetics in mDia1/3-depleted neurons, whereas endogenous vGAT
254 endocytosis was delayed upon expression of dominant-negative Rac1 (Rac1-DN) and loss of
255 mDia1/3 exacerbated this phenotype (Figure 6H and Figure 6-Supplement 1E). No overt effect of
256 overexpression of either Rac1 form on Syph-pH exocytosis was observed (Figure 6- Supplement
257 1F). Perturbation of the related Cdc42 protein, another actin regulatory GTPase (Lawson & Ridley,
258 2018) found at synapses (Figure 6- Supplement 1G-I), did not significantly affect the kinetics of
259 SV endocytosis in control or mDia1/3-depleted neurons (Figure 6- Supplement 1J,K). These data
260 suggest that interdependent mDia1/3 and Rac1-based pathways control SV endocytosis via
261 presynaptic actin.

262 We probed this model by analyzing the ultrastructure of synapses from hippocampal
263 neurons depleted of mDia1/3 or following inhibition of Rac1 activity. Synapses from mDia1/3-
264 depleted neurons displayed an accumulation of non-coated plasma membrane invaginations that
265 were found both in the vicinty of the active zone as well as distal from the synaptic contact area
266 (Figure 7A-C). Moreover, we observed elevated numbers of endosome-like vacuoles (ELVs) that
267 might serve as a donor membrane for SV reformation (Kononenko & Haucke, 2015; Kononenko

268 *et al.*, 2014; Watanabe *et al.*, 2014) as suggested by the observed reduction in SV numbers in
269 mDia-depleted neurons (compare Figure 2). A prominent accumulation of plasma membrane
270 invaginations (Figure 7-Supplement 1A) and endosome-like vacuoles (Figure 7-Supplement 1B)
271 was similarly found in hippocampal neurons from mDia1 KO mice. Inhibition of Rac1 function
272 by EHT 1864 also led to the accumulation of non-coated plasma membrane invaginations (Figure
273 7E,G), whereas the number of endosome-like vacuoles was not significantly altered (Figure 7E,
274 H). Pharmacological blockade of Rac1 activity in neurons depleted of mDia1/3 further increased
275 the number of plasma membrane invaginations and endosome-like vacuoles (Figure 7F,G,H).
276 mDia1/3 loss and Rac1 perturbation exhibited similar phenotypes with respect to the length and
277 width of tubular membrane invaginations (Figure 7-Supplement 1C,D).
278 Collectively, these findings demonstrate that mDia1/3-Rho and Rac1 signaling pathways
279 cooperatively act to facilitate presynaptic endocytosis and SV recycling.
280
281 **DISCUSSION**
282 We found that loss of mDia1 either alone or in conjunction with the closely related mDia3 isoform
283 slows the kinetics of SV endocytosis of exogenous pHluorin-tagged SV proteins and of
284 endogenous vGAT without perturbing exocytic SV fusion. These phenotypes are accompanied by
285 the accumulation of plasma membrane invaginations and vacuolar structures as well as an activity-
286 dependent reduction of the total SV pool (Figures 1, 2, and 7). Furthrmore, we observe that
287 interdependent mDia1/3-Rho and Rac1 signaling pathways cooperatively act to facilitate
288 presynaptic endocytosis (Figures 6 and 7). Several lines of evidence indicate that these endocytic
289 phenotypes are a consequence of perturbed presynaptic actin levels or dynamics. (i) Endogenous
290 presynaptic F-actin is reduced in mDia1/3-depleted hippocampal synapses (Figure 4) and (ii) actin
291 polymerization-defective mDia1 fails to restore normal endocytosis kinetics in hippocampal

292 neurons depleted of mDia1 (Figure 4). Conversely, (iii) pharmacological stabilization of F-actin
293 by jasplakinolide (Figure 4) or (iv) expression of constitutively-active Rac1 to drive compensatory
294 actin polymerization (for example via other formins and/ or ARP2/3) (Figure 6) rescues
295 endocytosis in mDia1/3-KD hippocampal neurons. Moreover, (v) we find mDia1 (Figure 3) and
296 F-actin (Figure 4) to accumulate at presynapses under conditions of impaired dynamin-dependent
297 endocytosis. Together with the observation that inhibition of F-actin dynamics (Peng *et al.*, 2011)
298 in the combined presence of latrunculin A, jasplakinolide, and Y-27632 (Figure 1) slows the
299 kinetics of SV endocytosis, our data support the hypothesis that presynaptic actin facilitates SV
300 endocytosis downstream of mDia/ RhoA and Rac1-based signaling pathways.

301 Our data extend previous studies using conditional genetics that have identified an actin
302 requirement for SV endocytosis (Wu *et al.*, 2016). The endocytic phenotype described here for
303 loss of mDia1/3, however, is substantially milder than that elicited by complete loss of β– or γ-
304 actin, likely reflecting the fact that several partially redundant pathways cooperate to promote
305 F-actin assembly at synapses (see below). In contrast to β- or γ-actin KO hippocampal neurons
306 (Wu *et al.*, 2016) we did not observe strong exocytic depression in response to train stimulation in
307 mDia-depleted neurons, although we cannot rule out mild differences in synaptic strength and/ or
308 release probability as observed in Rac1 KO hippocampal neurons and at the calyx of Held (Keine
309 *et al.*, 2022; O'Neil *et al.*, 2021).

310 At the ultrastructural level, we find that genetic (KO) or lentiviral induced (KD) loss of
311 mDia1 or mDia1/3 partially phenocopies acute perturbation of formin-mediated actin assembly
312 (Soykan *et al.*, 2017) with respect to the accumulation of plasma membrane invaginations. Unlike
313 acute formin inhibition (Soykan *et al.*, 2017), we find elevated numbers of post-fission endosome-
314 like vacuoles in mDia-depleted hippocampal synapses. The latter correlate with a mild reduction
315 of SV numbers, suggesting that mDia may have a further role in SV reformation downstream of

316 the actual endocytosis reaction (Chanaday *et al.*, 2019; Gan & Watanabe, 2018; Kononenko *et al.*,
317 2014). The identified function of mDia1/3-mediated presynaptic actin assembly in presynaptic
318 endocytosis and SV recycling is consistent with the actin binding properties of many endocytic
319 proteins including Dynamin (Ferguson *et al.*, 2009; Gu *et al*, 2014), PACSINs (Kessels &
320 Qualmann, 2006), or Epsins, among others (McMahon & Boucrot, 2011; Merrifield *et al.*, 2005;
321 Saheki & De Camilli, 2012). How exactly actin functions to facilitate endocytosis of SV
322 membranes remains to be fully understood. The comparably small size of the membrane
323 invaginations that accumulate following pharmacological inhibition of formins (< 100 nm) or Rac1
324 or upon genetic loss of mDia1 (typically < 150 nm, although larger ones are observed) render an
325 actomyosin-based constriction mechanism for SV endocytosis unlikely (consistent with
326 (Sankaranarayanan *et al.*, 2003)). We rather favor a - possibly indirect - function of F-actin in
327 presynaptic endocytosis via formation of an F-actin ring that couples exocytic membrane
328 compression to endocytic pit formation (Ogunmowo *et al.*, 2023). Such a model is supported by
329 the abundance of large plasma membrane invaginations distal from the active zone where SV
330 fusion occurs at synapses following mDia1/3 and Rac1 loss of function (Figure 7). Consistent with
331 this, it has been shown that mDia1 controls presynaptic membrane contractility (Deguchi *et al*,
332 2016), e.g. via the recently identified presynaptic actin corrals visualized in genome-engineered
333 rat hippocampal neurons (Bingham *et al*, 2023).

334 A key result from our study is the finding that presynaptic endocytosis is regulated by
335 interdependent, yet partially redundant signaling for F-actin assembly downstream of Rho and
336 Rac1, e.g. pathways known to control linear and branched F-actin networks (Lawson & Ridley,
337 2018; Muller *et al.*, 2020) that were shown to co-exist within hippocampal presynaptic boutons
338 (Bingham *et al.*, 2023). We demonstrate that loss of mDia1/3 or inhibition of Rho cause the
339 hyperactivation of the actin-promoting GTPase Rac1 and that dual loss of mDia1/3 loss and Rac1

340 function results in synergistic inhibitory effects with respect to presynaptic endocytosis and
341 ultrastructural defects (Figures 5-7). These findings suggest that the signaling network that
342 regulates presynaptic actin assembly may have been evolutionary selected for plasticity and
343 resilience. A resilient network for the control of actin dynamics at the presynapse may also help
344 to explain the partially contradicting results from drug-based manipulations of actin and actin
345 regulatory factors in different models of presynaptic neurotransmission reported in the past
346 (Bleckert *et al.*, 2012; Del Signore *et al.*, 2021; Hori *et al.*, 2022; Piriya Ananda Babu *et al.*, 2020;
347 Richards *et al*, 2004; Sankaranarayanan *et al.*, 2003; Shupliakov *et al.*, 2002; Wu & Chan, 2022;
348 Wu *et al.*, 2016). Moreover, accumulating evidence indicates that different pools of actin might be
349 differentially amenable to drug treatments (Bleckert *et al.*, 2012), e.g. as a consequence of the
350 association of actin filaments with molecules such as tropomyosin (Gormal *et al*, 2017) that render
351 them resistant to drugs, and/ or variations in the fraction of F-actin *vs*. monomeric actin pools
352 (Higashida *et al*, 2008), providing a possible explanation for previously discrepant results.

353 A number of open questions remain. We predict that presynaptic actin assembly via mDia/
354 Rho and Rac1 facilitates all forms of presynaptic endocytosis that operate on timescales of
355 milliseconds to seconds (Chanaday & Kavalali, 2018; Clayton & Cousin, 2009; Watanabe &
356 Boucrot, 2017) and at many types of synapses (e.g. small central synapses, ribbon synapses, the
357 neuromuscular junction), but further studies will be needed to test this hypothesis. We note that
358 fast endophilin-mediated endocytosis (FEME), a process with resemblance to endocytosis at
359 synapses (Watanabe & Boucrot, 2017), has been shown to be differentially regulated by actin and
360 Rho GTPase family members (Boucrot *et al*, 2015; Renard *et al*, 2015). At present we do not
361 understand if and how RhoA/B and Rac1 GTPase activation is nested into the SV cycle and
362 whether these GTPases operate at the same or different nanoscale sites and on the same or different
363 membranes. Future studies will be required to tackle these questions.

364 **MATERIALS AND METHODS**

Key Resources Table				
Reagent type (species) or resource	**Designation**	**Source or reference**	**Identifiers**	**Additional information**
genetic reagent (Mus musculus)	C57BL/6N wild type	Leibniz Research Institute for Molecular Pharmacology	RRID:IMSR_JAX:000664	
genetic reagent (Mus musculus)	mDia1 KO	Bartolini Lab, Columbia University	Peng et al., 2003; DOI: 10.1016/s0960-9822(03)00170-2	
cell line (Homo sapiens)	HEK293T	American Type Culture Collection	Cat# CRL-3216; RRID:CVCL_0063	
antibody	β-Actin (mouse monoclonal)	Sigma-Aldrich	Cat# A5441; RRID:AB_476744	IB (1:5000)
antibody	Bassoon (guinea pig monoclonal)	Synaptic Systems	Cat# 141 318; RRID:AB_2927388	IC (1:100)
antibody	CDC42 (rabbit polyclonal)	Abcam	Cat# ab64533; RRID:AB_1310067	IB (1:1000); IC (1:100)
antibody	Dynamin1 (rabbit polyclonal)	Pietro D. Camilli	Shupliakov et al., 1997; DOI: 10.1126/science.276.5310.259	IB (1:2000)
antibody	GFP (mouse monoclonal)	Thermo Fisher Scientific	Cat# A-11120; RRID:AB_221568	IC (1:2500)
antibody	Homer1 (mouse monoclonal)	Synaptic Systems	Cat# 160 011; RRID:AB_2120992	IC (1:200)

antibody	Homer1 (rabbit polyclonal)	Synaptic Systems	Cat# 160 003; RRID:AB_887730	IC (1:200)
antibody	LAMP1 (rabbit monoclonal)	Cell Signaling Technology	Cat# 9091; RRID:AB_2687579	IB (1:1000)
antibody	mDia1 (mouse monoclonal)	BD Biosciences	Cat# 610848; RRID:AB_398167	IB (1:500); IP (2µg)
antibody	mDia1 (rabbit monoclonal)	Abcam	Cat# ab129167; RRID:AB_11143749	IC (1:100)
antibody	mDia3 (rabbit polyclonal)	Sigma-Aldrich	Cat# HPA005647; RRID:AB_1078657	IB (1:1000)
antibody	Myosin IIb (mouse monoclonal)	Abcam	Cat# ab684; RRID:AB_305661	IC (1:100)
antibody	Myosin IIb (rabbit polyclonal)	Cell Signaling Technology	Cat# 3404; RRID:AB_126421	IB (1:2000)
antibody	Rac1 (mouse monoclonal)	BD Biosciences	Cat# 610650; RRID:AB_397977	IB (1:1000); IC (1:50)
antibody	RFP (rabbit polyclonal)	Takara Bio	Cat# 632496; RRID:AB_10013483	IC (1:500)
antibody	RhoA (rabbit monoclonal)	Cell Signaling Technology	Cat# 2117; RRID:AB_10693922	IB (1:1000); IC (1:100)
antibody	α-Tubulin (mouse monoclonal)	Sigma-Aldrich	Cat# T9026; RRID:AB_47759	IB (1:5000)
antibody	IgG control (mouse monoclonal)	Thermo Fisher Scientific	Cat# 31903; RRID:AB_10959891	IP (2 µg)

antibody	vGAT-CypHer5E (rabbit polyclonal)	Synaptic Systems	Cat# 131 103CpH; RRID:AB_2189809	Live-imaging (1:500)
antibody	Anti-mouse IgG Atto542 (donkey polyclonal)	Martin Lehmann	Gonschior et al., 2022; https://doi.org/10.1038/s41467-022-32533-4	IC (1:400)
antibody	Anti-rabbit IgG Atto542 (donkey polyclonal)	Martin Lehmann	Gonschior et al., 2022; https://doi.org/10.1038/s41467-022-32533-4	IC (1:400)
antibody	Anti-mouse Alexa Fluor™ 594 (goat polyclonal)	Thermo Fisher Scientific	Cat# A-11032; RRID:AB_2534091	IC (1:200)
antibody	Anti-rabbit Alexa Fluor™ 594 (goat polyclonal)	Thermo Fisher Scientific	Cat# A-11037; RRID:AB_2534095	IC (1:200)
antibody	Anti-guinea pig Atto647N (camelid monoclonal)	Synaptic Systems	Cat# N0602-At647N-S; RRID:AB_2744576	IC (1:200)
antibody	Anti-mouse Alexa Fluor™ 647 (goat polyclonal)	Thermo Fisher Scientific	Cat# A-21235; RRID:AB_2535804	IC (1:200)
antibody	Anti-mouse IRDye® 680RD (goat polyclonal)	LI-COR Biosciences	Cat# 925-68070; RRID:AB_2651128	IB (1:10000)
antibody	Anti-rabbit IRDye® 680RD (goat polyclonal)	LI-COR Biosciences	Cat# 926-68071; RRID:AB_10956166	IB (1:10000)
antibody	Anti-mouse IgG, IRDye® 800CW (goat polyclonal)	LI-COR Biosciences	Cat# 926-32210; RRID:AB_621842	IB (1:10000)

antibody	Anti-rabbit IgG, IRDye® 800CW (goat polyclonal)	LI-COR Biosciences	Cat# 926-32211; RRID:AB_621843)	IB (1:10000)
chemical compound, drug	Phalloidin-Alexa FluorTM 594	AAT Bioquest	Cat# ABD-23158	IC (1:1000)
recombinant DNA reagent	Synaptophysin-pHluorin	Leon Lagnado	Granseth et al., 2006; DOI: 10.1016/j.neuron.2006.08.029	Expresses rat Synaptophysin-2xpHluorin (inserted between Asn183 – Thr184) under a CMV promotor
recombinant DNA reagent	vGlut1-pHluorin	Volker Haucke	Bolz et al., 2023; DOI: 10.1016/j.neuron.2023.	Expresses rat vGlut1-pHluorin (inserted between Gly99 – Gly100) under a hSyn1 promotor; lentiviral plasmid
recombinant DNA reagent	mCherry	Clontech	Cat# 632523	Expresses mCherry under a CMV promotor
recombinant DNA reagent	mDia1-WT-mCherry	This study	-	Expresses mouse mDia1-WT-mCherry under a CMV promotor
recombinant DNA reagent	mDia1-ΔN -mCherry	This study	-	Expresses truncation (first 60 AA) variant of mouse mDia1-mCherry under a CMV promotor
recombinant DNA reagent	mDia1-WT-SNAP	This study	-	Expresses mouse mDia1-WT-SNAP under a hSyn1

				promotor; lentiviral plasmid
recombinant DNA reagent	mDia1-K994A-SNAP	This study	-	Expresses K994A variant of mDia1-SNAP under a hSyn1 promotor; lentiviral plasmid
recombinant DNA reagent	Dynamin1-WT-SNAP	This study	-	Expresses mouse Dynamin1-WT-SNAP under a hSyn1 promotor; lentiviral plasmid
recombinant DNA reagent	Dynamin1-K44A-SNAP	This study	-	Expresses K44A variant of mouse Dynamin1-SNAP under a hSyn1 promotor; lentiviral plasmid
recombinant DNA reagent	vGlut1-mCherry	Franck Polleux	Kwon et al., 2016; https://doi.org/10.1371/journal.pbio.1002516	Expresses rat vGlut1-mCherry under a CAG promotor
recombinant DNA reagent	RhoA-WT	Theofilos Papadopoulos	Reddy-Alla et al. 2010; https://doi.org/10.1111/j.1460-9568.2010.07149.x	Expresses human 3xHA-RhoA-WT under a CMV promotor
recombinant DNA reagent	RhoA-DN	Theofilos Papadopoulos	Reddy-Alla et al. 2010; https://doi.org/10.1111/j.1460-9568.2010.07149.x	Expresses T19N variant of human 3xHA-RhoA under a CMV promotor
recombinant DNA reagent	RhoB-WT	Harry Mellor	Mellor et al., 1998; https://doi.org/10.	Expresses human myc-RhoB-WT

			1074/jbc.273.9.4811	under a CMV promotor
recombinant DNA reagent	RhoB-DN	Harry Mellor	Mellor et al., 1998; https://doi.org/10.1074/jbc.273.9.4811	Expresses T19N variant of human myc-RhoB under a CMV promotor
recombinant DNA reagent	shCTR (transfected)	Sigma-Aldrich	Cat# SHC016	No murine targets
recombinant DNA reagent	shmDia1 (transfected)	Sigma-Aldrich	Cat# TRCN0000108685	Targets 3'UTR of NM_007858
recombinant DNA reagent	shRhoA (transfected)	Sigma-Aldrich	Cat# TRCN0000302388	Targets CDS of NM_016802
recombinant DNA reagent	shRhoB (transfected)	Sigma-Aldrich	Cat# TRCN0000294874	Targets CDS of NM_007483
recombinant DNA reagent	shCTRmiR	This study	-	Expresses rat Synaptophysin-2xpHluorin under a CMV promotor and shRNA embedded into a microRNA (shRNAmiR) with no murine targets
recombinant DNA reagent	shmDia1miR	This study	-	Expresses rat Synaptophysin-2xpHluorin under a CMV promotor and shRNAmiR against the CDS of mouse mDia1
recombinant DNA reagent	shCTR (transduced)	Christian Rosenmund	Watanabe et al., 2014;	Expresses NLS-RFP or BFP under a hSyn1 promotor

			https://doi.org/10.1038/nature13846	and shRNA against no murine target (msClathrin scrambled) under a U6 promotor
recombinant DNA reagent	shmDia1 (transduced)	This study	-	Expresses NLS-RFP or BFP under a hSyn1 promotor and shRNA against the 3'UTR of mouse mDia1 under a U6 promotor
recombinant DNA reagent	shmDia3 (transduced)	This study	-	Expresses NLS-RFP or BFP under a hSyn1 promotor and shRNA against the CDS of mouse mDia3 under a U6 promotor
recombinant DNA reagent	MD2.G	Addgene	Cat# 12259; RRID:Addgene_12259	Expresses lentiviral VSV-G envelope protein
recombinant DNA reagent	psPAX2	Addgene	Cat# 12260; RRID:Addgene_12260	Expresses lentiviral packaging protein
recombinant DNA reagent	pOrange GFP-β-Actin KI	Addgene	Cat#131479; RRID:Addgene_131479	gRNA and GFP donor for endogenous N-terminal tagging of β-Actin (amino acid position: D2)
chemical compound, drug	Dynasore	Sigma-Aldrich	Cat# D7693	80 µM 10 min

chemical compound, drug	EHT 1864	MedChemExpress	Cat# HY-16659	10 µM acute (CypHer); 2 h (IC/EM)
chemical compound, drug	IMM-01	Sigma-Aldrich	Cat# SML1064	10 µM acute
chemical compound, drug	Jasplakinolide	Sigma-Aldrich	Cat# J4580	8 µM acute (JLY); 1 µM 30 min
chemical compound, drug	Latrunculin A	Cayman Chemical	Cat# CAY10684	5 µM acute (JLY)
chemical compound, drug	ML141	MedChemExpress	Cat# HY-12755	10 µM acute
chemical compound, drug	Rhosin	MedChemExpress	Cat# HY-12646	10 µM 2 h
chemical compound, drug	Tetrodotoxin	Carl Roth	Cat# 6973.1	1 µM 36 h
chemical compound, drug	Y-27632	Tocris	Cat# 1254	1 µM acute (JLY)
commercial assay or kit	Rhotekin-Rho binding domain (RBD) beads	Cytoskeleton Inc.	Cat# RT02	60 µg
commercial assay or kit	PAK-p21 binding domain (PBD) beads	Cytoskeleton Inc.	Cat# PAK02	20 µg
commercial assay or kit	ProFection Mammalian Transfection System – Calcium Phosphate	Promega	Cat# E1200	
commercial assay or kit	Gibson Master Mix	New England Biolabs Inc.	Cat# E2611L	
commercial assay or kit	Q5 site-directed mutagenesis kit	New England Biolabs Inc.	Cat# E0552S	
software, algorithm	Fiji	NIH	RRID:SCR_002285	

software, algorithm	Prism	GraphPad	RRID:SCR_002798	Version 9.5.1.
software, algorithm	Image Lab Software	Bio-Rad	RRID:SCR_014210	Version 6.0.1
software, algorithm	Image Studio Lite	LI-COR Biosciences	RRID:SCR_013715	Version 5.2.5
software, algorithm	pHluorin ROI sector	Github	https://github.com/DennisVoll/pHluorin_ROI_selector/; RRID:SCR_002630	
software, algorithm	SynActJ	Martin Lehmann	Schmied et al., 2021; https://doi.org/10.3389/fcomp.2021.777837	
software, algorithm	Macro_plot_lineprofile_multicolor	Kees Straatman	F. Gerth et al., 2019; https://doi.org/10.1016/j.str.2019.03.020	
software, algorithm	MaxQuant	Jürgen Cox	https://www.maxquant.org/maxquant/	Version 1.6.1.0

Materials

Animals

Primary neurons were obtained from either wild-type C57BL/6J (Charles River, RRID: IMSR_JAX:000664) or mDia1 KO mice (Peng *et al.*, 2007; Peng *et al.*, 2003). All animal experiments were reviewed and approved by the ethics committee of the *Landesamt für Gesundheit und Soziales* (LAGeSo) Berlin or the Committee on the Ethics of Animal Experiments

372 of Columbia University and conducted according to the committees' guidelines (LAGeSo) or the
373 Guide for the Care and Use of Laboratory Animals of the National Institutes of Health (for mDia1
374 KO mice). At the facilities, animal care officers monitored compliance with all regulations. Mice
375 were group-housed under 12/12 h light/dark cycle with access to food and water *ad libitum*. Mice
376 from both genders were used and cultures were randomly allocated to experimental groups (e.g.,
377 different treatments). Multiple independent experiments using several biological replicates were
378 carried out as indicated in the figure legends.
379
380 **Antibodies**
381 Antibodies and their working dilutions used in this study are denoted in the Key Resource Table
382 (IB: Immunoblot; IC: Immunocytochemistry; IP: Immunoprecipitation). Antibodies were stored
383 according to the manufacturer's recommendations. All secondary antibodies are species-specific
384 (highly cross-adsorbed).
385
386 **Cell lines**
387 Human embryonic kidney 293T (HEK293T) cells were obtained from the American Type Culture
388 Collection (Cat# CRL-3216; RRID:CVCL_0063). Cells were cultured in Dulbecco's modified
389 Eagle's medium supplemented with glucose (DMEM; 4.5 g/L; Thermo Fisher Scientific) and 10%
390 heat-inactivated fetal bovine serum (FBS; Gibco), penicillin (100 U/ml; Gibco), and streptomycin
391 (100 µg/ml; Gibco) at 37°C and 5% CO_2. Cells were routinely tested for mycoplasma
392 contamination.
393
394 **Chemicals**

395 Compounds were dissolved in dimethyl sulfoxide (DMSO), unless indicated otherwise, and
396 diluted 1: 1000 to their working concentrations (s. Key Resource Table). For acute
397 pharmacological treatment (in pHluorin/CypHer assays), drugs were added to the imaging buffer.
398 For longer incubations, the conditioned cell media was supplemented with the chemicals (s. Key
399 Resource Table for incubation time).
400 For silencing neuronal network activity, sodium channels were inhibited by addition of
401 tetrodotoxin (TTX; in 10 mM sodium acetate, pH 5.3) to the neuronal culture medium at day in
402 vitro (DIV) 12 for 36 h. As a control, cells from the same preparation were treated with equal
403 volumes of 10 mM sodium acetate (annotated as Vehicle).
404
405 **Plasmids**
406 All recombinant DNA reagents used for protein expression are listed in the Key Resource Table:
407 Synaptophysin-pHluorin was a kind gift from Dr. L. Lagnado (Univ. of Sussex, UK), vGLUT1-
408 pHluorin was generated in-house by Svenja Bolz as previously described, while vGLUT1-
409 mCherry was kindly provided by Dr. Franck Polleux (New York, USA). HA-tagged RhoA-WT
410 and RhoA-T19N were kind gifts from Dr. Theofilos Papadopoulos (Göttingen, Germany) and
411 myc-tagged RhoB-WT and RhoB-T19N were kindly gifted by Dr. Harry Mellor (Bristol, UK). All
412 other expression vectors were generated for this study. Plasmids based on pEGFP-C1, pmCherry-
413 N1, pCAG and pcDNA3 utilising a CMV or CAG promotor (s. Key Resource table) were used for
414 overexpression based on transfection of neuronal cells, while pFUGW vectors carrying a human
415 Synapsin1 promotor (hSyn1) were used for the generation of lentiviral particles for the
416 transduction of neurons (s. Key Resource Table annotated as “lentiviral plasmid”). In the course
417 of this study several approaches to deplete mDia1 have been carried out and are annotated in the
418 figure legends: For knockdown of mDia1, RhoA and RhoB by transfection, commercially

419 available lentiviral small hairpin RNA (shRNA) vectors based on the pLKO.1 backbone (s. Key
420 Resource Table; annotated as "transfected") were purchased from Sigma-Aldrich. To reduce the
421 amount of DNA needed for transfection to perform pHluorin assays, vectors expressing shRNA
422 embedded into a microRNA (miRNA) context for mDia1 together with Synaptophysin-2x-
423 pHluorin as a reporter were cloned based on pRRLsinPPT-emGFP-miR Control, a kind gift of Dr.
424 Peter S. McPherson (Montreal, Canada). Finally, lentiviral vectors for knockdown of mDia1 and
425 mDia3 (annotated in Key Resource Table as "transduced") were generated based on the backbone
426 f(U6) sNLS-RFPw shCTR, a kind gift from Christian Rosenmund (Berlin, Germany). All vectors
427 used for genetic depletion via RNA interference are listed in the Key Resource Table and express
428 gene-specific shRNA under a U6 promotor, that either targets the coding sequence (CDS) or the
429 3'-untranslated region (3'-UTR).
430
431 **Oligonucleotides**
432 Plasmids generated for this study were cloned using oligonucleotides (BioTez GmbH, Berlin,
433 Germany) listed in Supporting Table 1 (lower case denotes nucleotides that do not anneal to the
434 backbone; underlined nucleotides denote sense and antisense sequences of shRNA).
435
436 **Methods**
437 **Generation of expression plasmids**
438 Expression plasmids generated for this study were cloned by PCR amplification (Phusion™ High-
439 Fidelity DNA polymerase) and restriction enzyme (Thermo Fisher Scientific; Fast digest) digest
440 according to the manufacturers' manual. pSNAP-N1 was generated in-house by Hannes Gonschior
441 by sub-cloning $pSNAP_f$ (New England BioLabs Inc., Cat#N9183S) via PCR and the restriction
442 enzymes *AgeI* and *NotI* into pmCherry-N1. pFUG_hSyn_MCS was cloned by Amirreza Ohadi to

443 enable simple insertion of SNAP-tagged proteins by inserting a multiple cloning site (MCS) on
444 annealed oligonucleotides into a pFUG_hSyn1 backbone (a gift from Christian Rosenmund,
445 Berlin, Germany) cut by *AgeI* and *EcoRI*. To generate mDia1-WT-mCherry, the coding sequence
446 of mDia1 was cut from mDia1-mEmerald-N1 (Addgene, Cat#54157) and pasted into pmCherry-
447 N1 by *AgeI* and *XhoI* digestion. mDia1-WT-SNAP was cloned by cutting out the coding sequence
448 of mDia1 from mDia1-mEmerald-N1 and pasting it into pSNAP-N1 by *AgeI* and *NheI* digest of
449 both vector and insert. To subclone mDia1-SNAP into a lentiviral vector the coding sequence of
450 mDia1-SNAP was pasted from mDia1-WT-SNAP-N1 into pFUG_hSyn1_MCS utilizing common
451 cut sites for *NheI* and *NotI* digest. For the generation of a lentiviral vector expressing Dynamin-
452 WT, the coding sequence of Dynamin1 was first extracted from Dynamin1-pmCherry-N1
453 (Addgene; Cat#27697) by *EcoRI* and *XmaI* digestion and cloned into pSNAP-N1 with the same
454 enzymes. Subsequently, Dynamin1-SNAP was isolated by *NheI* and *NotI* digest and transformed
455 into pFUG_hSyn1_MCS. The mDia1- ΔN truncation variant was generated by introducing a new
456 start codon on a primer shifted by 60 amino acids (s. Supporting Table 1), PCR amplifying the
457 truncated DNA and subcloning the template into pmCherry-N1 by *BglII* and *AgeI* digest. For
458 introducing point mutations in mDia1 (Lysine-994 to Alanine; K994A) and Dynamin1 (Lysine-44
459 to Alanine; K44A), the Q5 site-directed mutagenesis kit (New England Biolabs Inc.; E0552S) was
460 used according to the manufacturer's manual and oligonucleotides listed in Supporting Table 1.
461 All vectors were confirmed by Sanger sequencing (LGC Genomics, Berlin, Germany)
462 and amplified by self-made chemically competent TOP10 *E.coli* before purifying respective
463 endotoxin-free DNA by 2-propanole precipitation.
464
465 **Isolation, culture and transfection of primary hippocampal neurons**

466 Neuronal hippocampal cell cultures were prepared as described before (Lopez-Hernandez *et al.*,
467 2022; Soykan *et al.*, 2017). In short, hippocampi from postnatal mice (p0-p3) were surgically
468 isolated and dissociated into single cells by trypsin (5 g/L, Sigma-Aldrich) digestion. Neurons
469 (100000 cells/ well of a 6-well) were plated onto poly-L-lysine-coated coverslips and grown in
470 modified Eagle medium (MEM; Thermo Fisher) supplemented with 5% FCS and 2% B-27 (Gibco)
471 and maintained at 5% CO_2 and 37°C in humidified incubators. In addition, 2 µM cytosine β-D-
472 arabinofuranoside (AraC) was added to the cell culture media in the first 2 days in vitro (DIV) to
473 limit glial proliferation. For transient protein expression, neurons were transfected on DIV 7-9
474 utilizing a Calcium phosphate transfection kit (Promega; Cat# E1200): In brief, 1-6 µg plasmid
475 DNA (per well of a 6-well plate) were mixed with 250 mM calcium phosphate ($CaCl_2$) in ultrapure
476 nuclease-free water. The resulting solution was added to equal volumes of 2x 4-(2-hydroxyethyl)-
477 1-piperazineethanesulfonic acid buffered saline (2x HEPES; 100 µL) and incubated at room
478 temperature for 20 min. Resulting precipitates were added dropwise to cells that had been
479 transferred to osmolarity-adjusted Neurobasal-A (NBA; Gibco) media to induce starvation. After
480 incubation at 37°C and 5% CO_2 for 30 min, neurons were washed thrice with osmolarity-adjusted
481 Hank's balanced salt solutions (HBSS; Gibco) and transferred back to their original conditioned
482 media.
483
484 **shRNA cloning and lentivirus production**
485 Knockdown of proteins was achieved through RNA interference either by $CaCl_2$ transfection of
486 gene-specific shRNA encoding vectors (pLKO.1; Sigma-Aldrich or shRNAmiR) on DIV 7 or by
487 transduction of cells with lentiviral particles harboring the gene-specific shRNA on DIV 2. The
488 respective method is indicated in the figure legends as *transfected* or *transduced*. To reduce the
489 amount of DNA needed for transfection and to improve neuronal health, shRNAmiR were

490 expressed from the 3'UTR of Synaptophysin-pHluorin based on (Ritter *et al*, 2017): The reporter
491 protein/synthetic cassette was generated by PCR amplifying Synaptophysin-2x-pHluorin with
492 oligos (s. Supporting Table 1) harboring *XbaI* and *SalI* sites. The eGFP in the RRLsinPPT-eGFP-
493 miRCTR plasmid (a kind gift from Dr. Peter S. McPherson, McGill University, Canada) was
494 replaced by the PCR product through similar restriction digest to yield shCTRmiR. miRmDia1
495 (start position 4892, targeting sequence matches open-reading frame) was designed with BLOCK-
496 iT™ (Thermo Fisher Scientific) and subcloned into shCTRmiR to yield shmDia1miR following
497 protocol in (Ritter *et al.*, 2017).

498 As both transfection strategies were limited by low efficiency, lentiviral knockdown was
499 carried out: Lentiviral particles were based on a shuttle vector (pFUGw) driving the expression of
500 a nuclear-targeted red fluorescent protein (NLS-RFP) under a human Synapsin1 (hSyn1) promotor
501 to monitor infection efficiency in neurons and a scrambled mouse shRNA against Clathrin without
502 any murine targets, which was used as the control virus (f(U6) sNLS-RFPw shCTR). To prevent
503 crosstalk between the NLS-RFP and other mCherry constructs, a similar backbone expressing the
504 blue fluorescent protein (BFP) as a reporter was generated in house by Klaas Ypermann: The
505 backbone was digested by *XbaI* and *PacI*, the hSyn1 promotor and mTagBFP (Addgene; #Cat
506 105772) were amplified with oligos (s. Supporting Table 1), gel extracted and assembled utilizing
507 a Gibson master mix (New England BioLabs Inc.; Cat#E2611L) to yield f(U6) BFP shCTR. To
508 knockdown mDia1, a shRNA sequence based on 5'-GCCTAAATGGTCAAGGAGATA-3' as the
509 sense nucleotide corresponding to the 3'UTR of mouse mDia1 (NM_007858.4; Sigma-Aldrich,
510 Cat# TRCN0000108685) was designed as an oligonucleotide with overhangs (s. Supporting Table
511 1) and annealed into the f(U6) sNLS-RFPw shCTR backbone cut with *BamHI* and *PacI* to yield
512 the vector f(U6) sNLS-RFPw/BFP shmDia1. For mDia3 shRNA, a sense sequence based on 5'-
513 GCCCTAATCCAGAATCTTGTA-3' corresponding to nucleotides 2473-2493 of mouse mDia3

514 (DIAPH2; NM_172493.2; Sigma-Aldrich, Cat# TRCN0000108782) was used to construct f(U6)
515 sNLS-RFPw/BFP shmDia3 as described above. Production of lentiviral particles was conducted
516 using the second-generation packaging system: In brief, HEK293T were co-transfected with
517 lentiviral shRNA constructs and the packaging plasmids psPAX2 (Addgene; Cat# 12260) and
518 MD2.G (Addgene; Cat# 12259) using $CaCl_2$. After 12 h, the cell media was replaced. Virus-
519 containing supernatants were collected at 48 and 72 h after transfection, filtered to remove cell
520 debris and particles were concentrated (30-fold) via low-speed centrifugation (Amicon Ultra-15,
521 Ultracel-100; Merck Millipore; Cat# UFC9100) before aliquoting and storage at -70°C. For all
522 experiments, an infection rate of over 95% was achieved at DIV 14-16.
523
524 **Microscopy**
525 **Live-imaging of SV recycling**
526 For live-imaging of Synaptophysin and vesicular glutamate transporter 1 (vGLUT1) recycling, SV
527 proteins fused to the green-fluorescent protein-based pH-sensitive fluorescent reporter pHluorin at
528 their luminal domain were overexpressed by plasmid transfection (Synaptophysin-pHluorin; DIV
529 7) or lentiviral transduction (vGLUT1-pHluorin; DIV 2).
530 For following endogenous vesicular gamma-aminobutyric acid transporter (vGAT) recycling,
531 spontaneously active synaptic boutons were labeled by incubating cells with CypHer5E-
532 conjugated antibodies against the luminal domain of vGAT (1:500 from a 1 mg/ml stock; Synaptic
533 Systems; Cat#131,103CpH) for 2 h in their respective conditioned culture media at 37 °C and 5 %
534 CO_2 prior to imaging.
535 To investigate kinetics of SV recycling, neurons at DIV 14-16 were placed into an RC-
536 47FSLP stimulation chamber (Warner Instruments) in osmolarity-adjusted imaging buffer [170
537 mM sodium chloride (NaCl), 20 mM N-Tris(hydroxyl-methyl)-methyl-2-aminoethane-sulphonic

538 acid (TES), 5 mM Glucose, 5 mM sodium hydrogencabonate ($NaHCO_3$), 3.5 mM potassium
539 chloride (KCl), 1.3 mM $CaCl_2$, 1.2 mM sodium sulfate (Na_2SO_4), 1.2 mM magnesium chloride
540 ($MgCl_2$), 0.4 mM potassium dihydrogenphosphate (KH_2PO_4), 50 µM *(2R)*-amino-5-
541 phosphonovaleric acid (AP5) and 10 µM 6-cyano-7-nitroquinoxaline-2,3-dione (CNQX); pH 7.4]
542 at 37°C (Tempcontrol 37-2 digital). Cells were subjected to electrical field-stimulation (MultiStim
543 System-D330; Digimeter Ltd.) with annotated stimulation trains to evoke action potentials (APs)
544 [40 Hz, 5s (200 APs), 40 Hz, 2s (80 APs), 20 Hz, 2s (40 APs); at 100 mA]. Following changes in
545 fluorescence were tracked by an inverted Zeiss Axiovert 200M microscope, equipped with a 40x
546 oil-immersion EC Plan Neofluar objective (NA 1.30), an EM-CCD camera (Evolve Delta 512)
547 and a pE-300^{white} LED light source (CoolLED). The scanning format was set to 512 x 512 pixels
548 with 16-bit sampling. eGFP (Excitation: BP470-40; Emission: BP535-50; Zeiss filter set 38) or
549 Cy5 (Excitation: BP640-30; Emission: BP525-50; Zeiss filter set 50) filter sets were used for
550 pHluorin or CypHer assays, respectively. Images were acquired at 0.5 Hz frame rate for 100 s with
551 50 (Syph-pH) or 100 (vGLUT1-pH, vGAT-CypHer) ms exposure with an electron multiplying
552 gain of 250 operated through Fiji-based MicroManager 4.11 software.

553 Analysis of responding boutons was performed through custom written macros to identify
554 regions of interest (ROIs) (https://github.com/DennisVoll/pHluorin_ROI_selector/) in an
555 automated manner using SynActJ (Schmied *et al*, 2021). Such analysis averaged fluorescence for
556 each time point in an image series (video) of at least > 20 responding boutons and corrected values
557 for background fluorescence yielding raw background-corrected fluorescence (F). The fold
558 increase of fluorescence after stimulation (F_{max}) can serve as a measure for exocytic fusion and is
559 calculated by normalising F by the mean intensity of F before stimulation (Baseline/basal
560 fluorescence (F_0) = mean intensity of first 5 frames for pHluorin; first 10 frames for CypHer) for
561 each time point (surface normalisation = F/F_0). To account for boutons with varying pHluorin

562 expression in one image series and to compare reacidification kinetics, the fluorescence of each
563 time point was subtracted by the basal fluorescence (F_0) to yield ΔF ($F-F_0$), which was then
564 normalised by its peak value (ΔF_{max}). Resulting peak normalised curves ($\Delta F/ \Delta F_{max}$) are annotated
565 as norm. ΔF. Endocytic decay constants (τ) were calculated by averaging and then fitting the norm.
566 ΔF ($\Delta F/\Delta F_{max}$) traces of all videos in one condition (N) to a mono-exponential decay curve [$y_0 +$
567 $A*e^{(-t/\tau)}$] with the constraints of $y_0 = 1$ and offset = 0 in Prism 9 (Graphpad).
568 CypHer-traces had to be corrected for photobleaching: The decay constant of the bleaching curve
569 was determined by fitting the data points of the first 10 frames (20 s, prior to stimulation) to a
570 mono-exponential decay curve. The corresponding value of the photobleaching curve at a given
571 time *t* was added to the raw fluorescence intensity measured at each corresponding time point to
572 correct for the loss of intensity due to bleaching.
573
574 **Immunocytochemistry**
575 For immunostainings, neuronal cultures were chemically fixed on DIV 14-16 using 4 % p-
576 formaldehyde (PFA) and 4 % sucrose in phosphate buffered saline (PBS) for 15 min at room
577 temperature (RT). For experiments in figure 3G-H, cultures were stimulated with a 40 Hz train for
578 5 s in imaging buffer before immediate fixation. After fixation, cells were washed thrice with PBS
579 and incubated with permeabilization buffer (10% normal goat serum, 0.3 % Triton X-100 in PBS)
580 for 30 min at RT, followed by primary antibody incubation of proteins of interest in
581 permeabilization buffer at indicated dilutions (see Key Resource Table) at 4°C overnight.
582 Subsequently, unbound antibodies were removed by three PBS washes while bound antibodies
583 were decorated by corresponding fluorophore-coupled secondary antibodies in permeabilization
584 buffer for 1h at RT. For F-Actin staining, Phalloidin-Alexa Fluor™ 594 (1:1000 stock; AAT
585 Bioquest; Cat# ABD-23158) was added in the secondary incubation step. Finally, neurons were

586 washed thrice with PBS, followed by two washes with ultra-pure water. Coverslips were dried for
587 2 h before mounting in ProLong™ Gold Antifade (Thermo Fisher Scientific; #P36934) on glass
588 slides (Thermo Fisher Scientific; VWR; Cat#630-1985). The slides were cured for at least 72 h at
589 RT before imaging.
590
591 **Multicolor time-gated STED imaging**
592 STED images were acquired from fixed samples by a HC PL APO CS2 100 x oil objective (1.40
593 NA) on a Leica SP8 TCS STED 3x microscope (Leica Microsystems) equipped with a pulsed
594 white-light excitation laser (WLL; ~ 80 ps pulse width, 80 MHz repetition rate; NKT Photonics)
595 and a STED laser for depletion (775 nm). The scanning format was set to 1024 x 1024 pixels, with
596 8-bit sampling, 4x line averaging, 4x frame accumulation and 6 x optical zoom, yielding a final
597 pixel size of 18.9 nm. Three-color imaging was performed by sequentially exciting following
598 fluorophores (excitation filter = Exf; emission filter = Emf): Atto647N (Exf: 640 nm; Emf: 650-
599 700 nm); Alexa Fluor™ 594 (Exf: 590 nm; Emf: 600-640 nm) and Atto542 (Exf: 540 nm; Emf:
600 550-580 nm) operated by the Leica Application Suite X (Leica Microsystems, 2020). For
601 stimulated depletion of the signal, the 775 nm STED laser was applied to all emissions. Detection
602 of the resulting signal was time-gated by 0.3-6 ns to allow enough time for stimulated depletion
603 and collected by two sensitive HyD detectors at appropriate spectral regions distinct from the
604 STED laser wavelength. Settings in independent experiments were similar between conditions to
605 allow quantification of signals. Raw data obtained from three-channel time-gated STED (gSTED)
606 imaging were analyzed with Fiji. For analysis, only synapses oriented in the xy-plane exhibiting a
607 clear separation of Bassoon (presynapse) and Homer1 (postsynapse) clusters were taken into
608 account. To determine synaptic localisation and presynaptic levels of proteins of interest,
609 multicolor line profiles were measured: A line (1.0 µm length, 0.4 µm width) perpendicular to the

610 synaptic cleft (space between Bassoon & Homer1 cluster) was drawn (Gerth *et al.*, 2017) and
611 fluorescence intensity of all three channels along this line was measured using a Fiji Macro
612 (Macro_plot_lineprofile_multicolor; Dr. Kees Straatman, University of Leicester, UK). Resulting
613 profiles were aligned to the maximum Bassoon intensity, which was set to 0 nm. For localization
614 analysis, all three profiles were normalized to their maxima, which were set to 1. For quantification
615 of presynaptic protein levels, only the fractions of the non-normalized line profiles of proteins of
616 interest overlapping with the normalized averaged Bassoon distribution were integrated.
617 Intensities were normalized to controls (DMSO, shCTR, WT) which were set to 100.
618
619 **Imaging of endogenous β-Actin levels**
620 To visualize endogenous β-Actin levels, eGFP knockin following the ORANGE method was
621 performed (Willems *et al.*, 2020): Neurons were transfected with vGLUT1-mCherry (Franck
622 Polleux) and pOrange GFP-β-Actin KI (Addgene; Cat#131479) by $CaCl_2$ on DIV 2. Directly
623 following transfection, cells were transduced with shCTR or shmDia1+3 lentiviral particles
624 carrying BFP as a reporter to prevent crosstalk between mCherry and NLS-RFP expression.
625 Neuronal cultures were chemically fixed on DIV 15. After fixation, endogenous GFP and
626 overexpressed vGLUT1-mCherry intensities were enhanced by additional antibody (anti-GFP and
627 anti-RFP; see Key Resource Table) incubation according to the immunocytochemistry protocol
628 described above. Images of neurons were taken on the STED microscope with and without
629 stimulated depletion (confocal) with the same settings as indicated above. For analysis, confocal
630 images were filtered by Gaussian blur (sigma = 2 pixel) and auto-thresholded using Otsu's method.
631 Whenever confocal vGLUT1 signal co-localized with confocal Actin clusters, the area was chosen
632 as a ROI. Actin intensity was then measured in the ROI applied to the STED image. The intensities
633 of β-Actin were normalized to shCTR which was set to 100.

634

635 **Transmission electron microscopy**

636 To investigate synaptic effects of F-actin manipulations at the ultrastructural level, cells on
637 coverslips were chemically fixed with 2 % glutaraldehyde in cacodylat buffer (CDB; 0.1 M sodium
638 cacodylat) for 1 h at RT. Coverslips were washed thrice with CDB before osmification by 1 %
639 (w/v) osmium tetroxide (OsO_4) and 1.5 % (w/v) potassium hexacyanoferrat ($K_3Fe(CN)_6$) in CBD
640 for 1 h at 4°C. After postfixation, cells were stained with 1 % (w/v) uranyl acetate, dehydrated by
641 methanol gradients and finally embedded by epoxy resin (Sigma Aldrich; Cat# 45359) infiltration.
642 After polymerization (60°C, 30 h), coverslips were removed and ultra-thin (70 nm) sections were
643 cut and contrasted with 2 % (w/v) uranyl acetate and 80 mM lead citrate. 8-bit Images were
644 obtained on a Zeiss 900 transmission electron microscope equipped with Olympus MegaViewIII
645 or Olympus Morada G2 digital cameras at 30000 x magnification yielding a pixel size of 1.07 nm.
646 Subsequently, morphometry (density of synaptic vesicles, endosome-like vacuoles, clathrin-
647 coated vesicles, clathrin-coated pits and non-coated invaginations) was analyzed from synaptic
648 profiles with clearly distinguishable active zones and adjacent synaptic vesicles in a blinded
649 manner.

650

651 **Biochemistry**

652 **Immunoblotting**

653 To compare protein levels between experimental conditions, immunoblotting was performed:
654 Protein concentrations in lysates were measured by BCA assay (Thermo Fisher Scientific;
655 Cat#23227) and equal protein amounts were diluted in Laemmli sample buffer [final (1 x)
656 concentration: 31.5 mM 2-Amino-2-(hydroxymethyl)propane-1,3-diol (Tris), 1 % (w/v) sodium
657 dodecyl sulfate (SDS), 10 % (v/v) glycerol, 0.001% (w/v) 3,3-Bis(3,5-dibromo-4-hydroxyphenyl)-

658 2,1λ^6-benzoxathiole-1,1(3*H*)-dione (bromophenol blue), 5 % (v/v) 2-mercaptoethanol; pH 6.8]
659 and denatured at 55°C for 20 min (unless indicated otherwise). Samples were resolved by SDS-
660 polyacrylamide gel electrophoresis (SDS-PAGE) with self-made Bis(2-hydroxyethyl)amino-
661 tris(hydroxymethyl)methan (BisTris; 250 mM) based 4-20 % polyacrylamide (Rotiphorese Gel
662 30; Carl Roth) gradient gels and run (80-120 V; 90 min) in NuPAGE MOPS SDS running buffer
663 (Thermo Fisher Scientific; Cat#NP000102) using Mini-PROTEAN Tetra Vertical Electrophoresis
664 Cells (Bio-Rad, Cat#1658004). For membrane fractionation experiments, RFP-fluorescence of
665 mDia1 variants in respective fractions was imaged in-gel on a ChemiDoc XRS+ (Bio-Rad)
666 controlled by the Image Lab software (version 6.0.1) utilizing the Alexa546 preset (605/50 Filter3;
667 Light Green Epi illumination). Separated proteins were wet-blotted (110 V; 90 min; 4°C) on
668 fluorescence-optimized polyvinylidene difluoride (PVDF) membranes (Immobilon-FL; Merck;
669 IPFL00010) in transfer buffer (25 mM Tris (pH 7.6), 192 mM glycine, 20% (v/v) methanol, 0.03%
670 (w/v) SDS). Subsequently, membranes were blocked with blocking buffer [5 % bovine serum
671 albumin (BSA), in Tris-buffered saline (TBS) containing 0.01% Tween 20 (TBS-T)] for 1 h at RT
672 and incubated (4 °C; overnight) with primary antibodies under constant agitation at indicated
673 dilutions (s. Key Resource Table) in blocking buffer. Membranes were washed thrice with TBS-T
674 and incubated with corresponding pairs of IRDye 680RD- or 800CW-conjugated secondary
675 antibodies in TBS-T for 1 h at RT. After three washes with TBS-T, bound antibodies were
676 visualized by the Odyssey Fc Imaging System (LI-COR Biosciences) controlled and analyzed by
677 Image Studio Lite (Version 5.2.5). For colorimetric analysis of protein levels, intensity of bands
678 was measured by assigning shapes of equal size to all lanes at similar heights and subtracting the
679 individual background for each shape. Signals were normalized to controls on the same blot. The
680 PageRuler Prestained (Thermo Fisher Scientific; Cat#26616) was used as a ladder to control for
681 protein size.

682

683 **Immunoprecipitation from synaptosomes**

684 To immunoprecipitate synaptic mDia1, synaptosomes (P2') were prepared as follows: One mouse
685 brain (p28) was homogenized (900 rpm; 12 strokes with glass-teflon homogenizer) in 7 mL of ice-
686 cold homogenization buffer [(320 mM sucrose, 4 mM HEPES; pH 7.4) supplemented with
687 mammalian protease inhibitor cocktail (PIC)] at 4°C. Large cellular debris and nuclei were
688 sedimented by centrifugation at 900 g for 10 min at 4°C. The supernatant was further centrifuged
689 at 12500 g for 15 min at 4°C. The resulting pellet (P2) was resuspended in 15 mL of
690 homogenization buffer and pelleted at 12500 g for 15 min at 4°C yielding the crude synaptosomal
691 fraction P2'. Subsequently, the pellet was resuspended in 2 mL of immunoprecipitation buffer [20
692 mM HEPES, 130 mM NaCl, 2 mM $MgCl_2$, 1 % (w/v)
693 3-[Dimethyl[3-(3α,7α,12α-trihydroxy-5β-cholan-24-amido)propyl]azaniumyl]propane-1-
694 sulfonate (CHAPS), PIC, phosphatase inhibitor cocktail II and III (Sigma-Aldrich); pH 7.4] and
695 lysed for 30 min at 4°C under light agitation. The lysate was cleared by centrifugation at 15000 g
696 at 4°C and protein concentration was measured using the BCA assay.

697 For identification of the protein environment of mDia1, P2' lysate (2 mg; 2 g/L) was
698 incubated with either 2 µg of anti-mDia1 antibody (BD Biosciences, Cat# 610848) or equal
699 amounts of immunoglobulin G (IgG) isotype control mouse antibody (Thermo Fisher Scientific;
700 Cat# 31903; RRID:AB_10959891) for 1 h at 4°C before the addition of 25 µL of Pierce Protein
701 A/G Magnetic Beads (Thermo Fisher Scientific) for an additional 2 h under constant rotation.
702 Subsequently, unbound proteins were removed from the beads by three consecutive wash cycles
703 with immunoprecipitation buffer. Bound proteins were eluted and boiled (10 min; 95°C) in 2x
704 Laemmli buffer, resolved by SDS-PAGE and analyzed by immunoblotting.

705

706 **LC-MS analysis of protein environment of mDia1**

707 For the analysis of interaction partners of synaptic mDia1, mDia1 was immunoprecipitated from
708 synaptosomes as described above. Eluted proteins were reduced (5 mM dithiothreitol; 30 min at
709 55°C), alkylated (15 mM iodoacetamide; 20 min at RT in the dark), and submitted to LC-MS
710 analysis: Proteins were subjected to SDS-PAGE following excision of 3 bands per lane and in-gel
711 digestion of proteins by trypsin (1:100 (w/w); overnight at 37°C). Resulting tryptic peptides were
712 separated by reverse-phase high-performance liquid chromatography (RP-HPLC; Ultimate™
713 3000 RSLCnano system; Thermo Scientific) using a 50 cm analytical column (in-house packed
714 with Poroshell 120 EC-C18; 2.7 µm; Agilent Technologies) with a 120 min gradient. RP-HPLC
715 was coupled on-line to an Orbitrap Elite mass spectrometer (Thermo Fisher Scientific) that
716 performed precursor ion (MS1) scans at a mass resolution of 60000, while fragment ion (MS2)
717 scans were acquired with an automatic gain control (AGC) target of 5 x 10^3 and a maximum
718 injection time of 50 ms. Data analysis including label free quantification was performed with
719 MaxQuant (version 1.6.1.0) using the following parameters: The initial maximum mass deviation
720 of the precursor ions was set at 4.5 parts per million (ppm), and the maximum mass deviation of
721 the fragment ions was set at 0.5 Da. Cysteine carbamidometyl and propionamide, Methionine
722 oxidation and N-terminal acetylation were set as variable modifications. For identification of
723 proteins, data were searched against the SwissProt murine database (Mouse_2016oktuniprot-
724 proteome%3AUP000000589.fasta). False discovery rates were < 1 % at the protein level based on
725 matches to reversed sequences in the concatenated target-decoy database. The statistical analysis
726 was done with Perseus (version 1.6.7.0).

727

728 **Effector pulldown assays**

729 To analyze the activity of small Rho GTPases, pulldowns utilizing effector protein domains which
730 exclusively bind to their GTP-bound forms were performed: Neurons (200 000 cells) were washed
731 with ice-cold PBS and harvested in GTPase lysis buffer (50 mM HEPES, 500 mM NaCl, 10mM
732 $MgCl_2$, PIC, phosphatase Inhibitor cocktails II + III; pH 7.4). Cells were lysed for 5 min under
733 repetitive mixing before centrifugation (15000 g; 5 min; 4°C). Cleared lysates were incubated with
734 Rhotekin-Rho binding domain (RBD) beads (60 µg; Cytoskeleton Inc.) or with PAK-p21 binding
735 domain (PBD) beads (20 µg; Cytoskeleton Inc.) at 4°C under constant rotation to bind active RhoA
736 or Cdc42 and Rac1, respectively. After 2 h, the beads were pelleted by centrifugation (1000 g; 1
737 min; 4°C) and washed with washing buffer (50 mM HEPES, 150 mM NaCl, 10 mM $MgCl_2$; pH
738 7.4). After repeated centrifugation, unbound proteins were discarded with the supernatant, while
739 bound proteins were eluted from the beads by addition of 2 x Laemmli buffer and boiling (10 min;
740 95°C). Finally, activity of small Rho GTPases was resolved by SDS-PAGE and analyzed by
741 immunoblotting input and pulldown samples.
742
743 **Membrane fractionation**
744 To characterize membrane association of the truncation mDia1 mutant, HEK293T cells were
745 transfected with wild-type (mDia1-WT) or mDia1 truncation mutant (mDia1-ΔN) using $CaCl_2$.
746 48 h after transfection cells were washed with ice-cold PBS and harvested in ice-cold resuspension
747 buffer (20 mM HEPES, 130 mM NaCl, PIC; pH 7.4). Cells were lysed by forcing the suspension
748 through 18-gauge syringes to crack the plasma membrane in between three freeze-thaw cycles in
749 liquid nitrogen. Nuclei were removed by centrifugation at 1000 g for 5 min at 4°C. The supernatant
750 (total lysate) was sedimented at 100000 g for 30 min at 4°C to yield the membrane fraction as the
751 pellet and the cytosolic fraction as the high-speed supernatant. The pellet was resuspended in
752 resuspension buffer to the same volume of the cytosolic fraction. Equal volumes of all fractions

753 were analyzed by SDS-PAGE and immunoblotting to allow interpretation of protein enrichment
754 in cytosolic or membrane fractions with respect to the total lysate.
755
756 **Statistical analysis**
757 All data in this study are presented as the mean ± standard error of the mean (SEM) and was
758 obtained from *N* independent experiments with a total sample number of *n* (e.g., number of images,
759 videos, synapses, etc.) as annotated in the figure legends. For analysis of protein levels in STED
760 microscopy and synaptic structures in EM, statistical differences between groups were calculated
761 considering *n*, while in all other experiments statistical differences were calculated between
762 independent experiments *N* (In pHluorin/CypHer assays, at least 20 responding boutons/video
763 were analyzed). For n > 100 or N > 5, data were tested for Gaussian distribution following
764 D'Agostino-Pearson tests to determine parametric versus non-parametric statistical testing. The
765 statistical significance between two groups was evaluated with either two-tailed unpaired student's
766 t-tests for normally distributed data or two-tailed unpaired Mann-Whitney tests, if data did not
767 follow Gaussian distribution. In experiments that necessitated normalization (to 100 or 1) before
768 analysis, one-sample t-tests or one-sample Wilcoxon rank tests were performed for normal and
769 non-normal distributed data, respectively. The statistical significance between more than two
770 experimental groups of normally distributed data was analyzed by one-way ANOVA, followed by
771 a Tukey's post hoc test, while Kruskal-Wallis tests with post hoc Dunn's multiple comparison test
772 were used when datasets did not follow Gaussian distribution.
773 Corresponding statistical tests are indicated in the figure and significance levels are
774 annotated as asterisks (*p < 0.05, **p < 0.01, ***p < 0.001, and ****p < 0.0001). Differences that
775 are not significant are not stated or indicated as ns (p > 0.05). Statistical data evaluation was

776 performed using GraphPad Prism 9.5.1 (733) and all calculated p-values are annotated in the
777 source data table. All figures were assembled using Affinity Designer (version 1.10.6.1665).
778
779 **Data availability**
780 All data generated and analyzed in this study are included in the manuscript and supporting files.
781 Numerical data as well as raw images of western blots are provided as source data files. Values
782 from the same experiment (N) are shaded in similar colors.
783
784 **Contact for Reagent and Resource Sharing**
785 Further information and requests for resources and reagents should be directed to and will be
786 fulfilled by the corresponding contact V.H. (Haucke@fmp-berlin.de).
787
788 **ACKNOWLEDGEMENTS**
789 We are indebted to Sabine Hahn, Delia Löwe and Silke Zillmann for expert technical assistance
790 with the preparation of neuronal cultures. We further wish to thank Dr. Martin Lehmann (FMP,
791 Berlin), Hannah Gelhaus and Gresy Bregu (both FU Berlin) for aid with STED imaging, Dr.
792 Dmytro Puchkov (FMP Imaging Core Facility) for supervising electron microscopy analysis, and
793 Heike Stephanowitz and Prof. Fan Liu (FMP Core Facility Proteomics) for proteomic analyses.
794 Supported by grants from the Deutsche Forschungsgemeinschaft (SFB958/ TP A01) to V.H..
795

796 **REFERENCES**

797 Anes E, Kuhnel MP, Bos E, Moniz-Pereira J, Habermann A, Griffiths G (2003) Selected lipids
798 activate phagosome actin assembly and maturation resulting in killing of pathogenic mycobacteria.
799 *Nat Cell Biol* 5: 793-802

800 Bingham D, Jakobs CE, Wernert F, Boroni-Rueda F, Jullien N, Schentarra EM, Friedl K, Da Costa
801 Moura J, van Bommel DM, Caillol G *et al* (2023) Presynapses contain distinct actin
802 nanostructures. *J Cell Biol* 222

803 Bleckert A, Photowala H, Alford S (2012) Dual pools of actin at presynaptic terminals. *J*
804 *Neurophysiol* 107: 3479-3492

805 Bloom O, Evergren E, Tomilin N, Kjaerulff O, Low P, Brodin L, Pieribone VA, Greengard P,
806 Shupliakov O (2003) Colocalization of synapsin and actin during synaptic vesicle recycling. *J Cell*
807 *Biol* 161: 737-747

808 Borst JG, Soria van Hoeve J (2012) The calyx of Held synapse: from model synapse to auditory
809 relay. *Annu Rev Physiol* 74: 199-224

810 Boucrot E, Ferreira AP, Almeida-Souza L, Debard S, Vallis Y, Howard G, Bertot L, Sauvonnet
811 N, McMahon HT (2015) Endophilin marks and controls a clathrin-independent endocytic
812 pathway. *Nature* 517: 460-465

813 Boulant S, Kural C, Zeeh JC, Ubelmann F, Kirchhausen T (2011) Actin dynamics counteract
814 membrane tension during clathrin-mediated endocytosis. *Nat Cell Biol* 13: 1124-1131

815 Chanaday NL, Cousin MA, Milosevic I, Watanabe S, Morgan JR (2019) The Synaptic Vesicle
816 Cycle Revisited: New Insights into the Modes and Mechanisms. *J Neurosci* 39: 8209-8216

817 Chanaday NL, Kavalali ET (2018) Optical detection of three modes of endocytosis at hippocampal
818 synapses. *Elife* 7

819 Chandrasekar I, Huettner JE, Turney SG, Bridgman PC (2013) Myosin II regulates activity
820 dependent compensatory endocytosis at central synapses. *J Neurosci* 33: 16131-16145
821 Chauhan BK, Lou M, Zheng Y, Lang RA (2011) Balanced Rac1 and RhoA activities regulate cell
822 shape and drive invagination morphogenesis in epithelia. *Proc Natl Acad Sci U S A* 108: 18289-
823 18294
824 Chen X, Wu X, Wu H, Zhang M (2020) Phase separation at the synapse. *Nat Neurosci* 23: 301-
825 310
826 Cingolani LA, Goda Y (2008) Actin in action: the interplay between the actin cytoskeleton and
827 synaptic efficacy. *Nat Rev Neurosci* 9: 344-356
828 Clayton EL, Cousin MA (2009) The molecular physiology of activity-dependent bulk endocytosis
829 of synaptic vesicles. *J Neurochem* 111: 901-914
830 Colgan LA, Yasuda R (2014) Plasticity of dendritic spines: subcompartmentalization of signaling.
831 *Annu Rev Physiol* 76: 365-385
832 Dani A, Huang B, Bergan J, Dulac C, Zhuang X (2010) Superresolution imaging of chemical
833 synapses in the brain. *Neuron* 68: 843-856
834 Daou P, Hasan S, Breitsprecher D, Baudelet E, Camoin L, Audebert S, Goode BL, Badache A
835 (2014) Essential and nonredundant roles for Diaphanous formins in cortical microtubule capture
836 and directed cell migration. *Mol Biol Cell* 25: 658-668
837 Deguchi Y, Harada M, Shinohara R, Lazarus M, Cherasse Y, Urade Y, Yamada D, Sekiguchi M,
838 Watanabe D, Furuyashiki T *et al* (2016) mDia and ROCK Mediate Actin-Dependent Presynaptic
839 Remodeling Regulating Synaptic Efficacy and Anxiety. *Cell Rep* 17: 2405-2417
840 Del Signore SJ, Kelley CF, Messelaar EM, Lemos T, Marchan MF, Ermanoska B, Mund M, Fai
841 TG, Kaksonen M, Rodal AA (2021) An autoinhibitory clamp of actin assembly constrains and
842 directs synaptic endocytosis. *Elife* 10

843 Delvendahl I, Vyleta NP, von Gersdorff H, Hallermann S (2016) Fast, Temperature-Sensitive and
844 Clathrin-Independent Endocytosis at Central Synapses. *Neuron* 90: 492-498
845 Eisenmann KM, Peng J, Wallar BJ, Alberts AS (2005) Rho GTPase-formin pairs in cytoskeletal
846 remodelling. *Novartis Found Symp* 269: 206-218; discussion 219-230
847 Engqvist-Goldstein AE, Drubin DG (2003) Actin assembly and endocytosis: from yeast to
848 mammals. *Annu Rev Cell Dev Biol* 19: 287-332
849 Ferguson SM, Brasnjo G, Hayashi M, Wolfel M, Collesi C, Giovedi S, Raimondi A, Gong LW,
850 Ariel P, Paradise S *et al* (2007) A selective activity-dependent requirement for dynamin 1 in
851 synaptic vesicle endocytosis. *Science* 316: 570-574
852 Ferguson SM, Raimondi A, Paradise S, Shen H, Mesaki K, Ferguson A, Destaing O, Ko G,
853 Takasaki J, Cremona O *et al* (2009) Coordinated actions of actin and BAR proteins upstream of
854 dynamin at endocytic clathrin-coated pits. *Dev Cell* 17: 811-822
855 Gan Q, Watanabe S (2018) Synaptic Vesicle Endocytosis in Different Model Systems. *Front Cell*
856 *Neurosci* 12: 171
857 Ganguly A, Tang Y, Wang L, Ladt K, Loi J, Dargent B, Leterrier C, Roy S (2015) A dynamic
858 formin-dependent deep F-actin network in axons. *J Cell Biol* 210: 401-417
859 Gerth F, Japel M, Pechstein A, Kochlamazashvili G, Lehmann M, Puchkov D, Onofri F, Benfenati
860 F, Nikonenko AG, Fredrich K *et al* (2017) Intersectin associates with synapsin and regulates its
861 nanoscale localization and function. *Proc Natl Acad Sci U S A* 114: 12057-12062
862 Goode BL, Eck MJ (2007) Mechanism and function of formins in the control of actin assembly.
863 *Annu Rev Biochem* 76: 593-627
864 Gormal R, Valmas N, Fath T, Meunier F (2017) A role for tropomyosins in activity-dependent
865 bulk endocytosis? *Mol Cell Neurosci* 84: 112-118

866 Gu C, Chang J, Shchedrina VA, Pham VA, Hartwig JH, Suphamungmee W, Lehman W, Hyman
867 BT, Bacskai BJ, Sever S (2014) Regulation of dynamin oligomerization in cells: the role of
868 dynamin-actin interactions and its GTPase activity. *Traffic* 15: 819-838
869 Higashi T, Ikeda T, Shirakawa R, Kondo H, Kawato M, Horiguchi M, Okuda T, Okawa K, Fukai
870 S, Nureki O *et al* (2008) Biochemical characterization of the Rho GTPase-regulated actin assembly
871 by diaphanous-related formins, mDia1 and Daam1, in platelets. *J Biol Chem* 283: 8746-8755
872 Higashida C, Suetsugu S, Tsuji T, Monypenny J, Narumiya S, Watanabe N (2008) G-actin
873 regulates rapid induction of actin nucleation by mDia1 to restore cellular actin polymers. *J Cell*
874 *Sci* 121: 3403-3412
875 Hodge RG, Ridley AJ (2016) Regulating Rho GTPases and their regulators. *Nature reviews*
876 *Molecular cell biology* 17: 496-510
877 Hori T, Eguchi K, Wang HY, Miyasaka T, Guillaud L, Taoufiq Z, Mahapatra S, Yamada H, Takei
878 K, Takahashi T (2022) Microtubule assembly by tau impairs endocytosis and neurotransmission
879 via dynamin sequestration in Alzheimer's disease synapse model. *Elife* 11
880 Hua Y, Sinha R, Thiel CS, Schmidt R, Huve J, Martens H, Hell SW, Egner A, Klingauf J (2011)
881 A readily retrievable pool of synaptic vesicles. *Nat Neurosci* 14: 833-839
882 Imoto Y, Raychaudhuri S, Ma Y, Fenske P, Sandoval E, Itoh K, Blumrich EM, Matsubayashi HT,
883 Mamer L, Zarebidaki F *et al* (2022) Dynamin is primed at endocytic sites for ultrafast endocytosis.
884 *Neuron* 110: 2815-2835 e2813
885 Keine C, Al-Yaari M, Radulovic T, Thomas CI, Valino Ramos P, Guerrero-Given D, Ranjan M,
886 Taschenberger H, Kamasawa N, Young SM, Jr. (2022) Presynaptic Rac1 controls synaptic
887 strength through the regulation of synaptic vesicle priming. *Elife* 11
888 Kessels MM, Qualmann B (2006) Syndapin oligomers interconnect the machineries for endocytic
889 vesicle formation and actin polymerization. *J Biol Chem* 281: 13285-13299

890 Kitzing TM, Sahadevan AS, Brandt DT, Knieling H, Hannemann S, Fackler OT, Grosshans J,
891 Grosse R (2007) Positive feedback between Dia1, LARG, and RhoA regulates cell morphology
892 and invasion. *Genes Dev* 21: 1478-1483
893 Kononenko NL, Haucke V (2015) Molecular mechanisms of presynaptic membrane retrieval and
894 synaptic vesicle reformation. *Neuron* 85: 484-496
895 Kononenko NL, Puchkov D, Classen GA, Walter AM, Pechstein A, Sawade L, Kaempf N,
896 Trimbuch T, Lorenz D, Rosenmund C *et al* (2014) Clathrin/AP-2 mediate synaptic vesicle
897 reformation from endosome-like vacuoles but are not essential for membrane retrieval at central
898 synapses. *Neuron* 82: 981-988
899 Lash LL, Wallar BJ, Turner JD, Vroegop SM, Kilkuskie RE, Kitchen-Goosen SM, Xu HE, Alberts
900 AS (2013) Small-molecule intramimics of formin autoinhibition: a new strategy to target the
901 cytoskeletal remodeling machinery in cancer cells. *Cancer Res* 73: 6793-6803
902 Lawson CD, Ridley AJ (2018) Rho GTPase signaling complexes in cell migration and invasion. *J*
903 *Cell Biol* 217: 447-457
904 Lopez-Hernandez T, Takenaka KI, Mori Y, Kongpracha P, Nagamori S, Haucke V, Takamori S
905 (2022) Clathrin-independent endocytic retrieval of SV proteins mediated by the clathrin adaptor
906 AP-2 at mammalian central synapses. *Elife* 11
907 Macia E, Ehrlich M, Massol R, Boucrot E, Brunner C, Kirchhausen T (2006) Dynasore, a cell-
908 permeable inhibitor of dynamin. *Dev Cell* 10: 839-850
909 Marston DJ, Dickinson S, Nobes CD (2003) Rac-dependent trans-endocytosis of ephrinBs
910 regulates Eph-ephrin contact repulsion. *Nat Cell Biol* 5: 879-888
911 McMahon HT, Boucrot E (2011) Molecular mechanism and physiological functions of clathrin-
912 mediated endocytosis. *Nature reviews Molecular cell biology* 12: 517-533

913 Merrifield CJ, Perrais D, Zenisek D (2005) Coupling between clathrin-coated-pit invagination,
914 cortactin recruitment, and membrane scission observed in live cells. *Cell* 121: 593-606
915 Miesenbock G, De Angelis DA, Rothman JE (1998) Visualizing secretion and synaptic
916 transmission with pH-sensitive green fluorescent proteins. *Nature* 394: 192-195
917 Muller PM, Rademacher J, Bagshaw RD, Wortmann C, Barth C, van Unen J, Alp KM, Giudice
918 G, Eccles RL, Heinrich LE *et al* (2020) Systems analysis of RhoGEF and RhoGAP regulatory
919 proteins reveals spatially organized RAC1 signalling from integrin adhesions. *Nat Cell Biol* 22:
920 498-511
921 O'Neil SD, Racz B, Brown WE, Gao Y, Soderblom EJ, Yasuda R, Soderling SH (2021) Action
922 potential-coupled Rho GTPase signaling drives presynaptic plasticity. *Elife* 10
923 Ogunmowo TH, Jing H, Raychaudhuri S, Kusick GF, Imoto Y, Li S, Itoh K, Ma Y, Jafri H, Dalva
924 MB *et al* (2023) Membrane compression by synaptic vesicle exocytosis triggers ultrafast
925 endocytosis. *Nat Commun* 14: 2888
926 Otomo T, Otomo C, Tomchick DR, Machius M, Rosen MK (2005) Structural basis of Rho
927 GTPase-mediated activation of the formin mDia1. *Mol Cell* 18: 273-281
928 Peng GE, Wilson SR, Weiner OD (2011) A pharmacological cocktail for arresting actin dynamics
929 in living cells. *Mol Biol Cell* 22: 3986-3994
930 Peng J, Kitchen SM, West RA, Sigler R, Eisenmann KM, Alberts AS (2007) Myeloproliferative
931 defects following targeting of the Drf1 gene encoding the mammalian diaphanous related formin
932 mDia1. *Cancer Res* 67: 7565-7571
933 Peng J, Wallar BJ, Flanders A, Swiatek PJ, Alberts AS (2003) Disruption of the Diaphanous-
934 related formin Drf1 gene encoding mDia1 reveals a role for Drf3 as an effector for Cdc42. *Curr*
935 *Biol* 13: 534-545

936 Piriya Ananda Babu L, Wang HY, Eguchi K, Guillaud L, Takahashi T (2020) Microtubule and
937 Actin Differentially Regulate Synaptic Vesicle Cycling to Maintain High-Frequency
938 Neurotransmission. *J Neurosci* 40: 131-142
939 Raimondi A, Ferguson SM, Lou X, Armbruster M, Paradise S, Giovedi S, Messa M, Kono N,
940 Takasaki J, Cappello V *et al* (2011) Overlapping role of dynamin isoforms in synaptic vesicle
941 endocytosis. *Neuron* 70: 1100-1114
942 Ramalingam N, Zhao H, Breitsprecher D, Lappalainen P, Faix J, Schleicher M (2010)
943 Phospholipids regulate localization and activity of mDia1 formin. *Eur J Cell Biol* 89: 723-732
944 Renard HF, Simunovic M, Lemiere J, Boucrot E, Garcia-Castillo MD, Arumugam S, Chambon V,
945 Lamaze C, Wunder C, Kenworthy AK *et al* (2015) Endophilin-A2 functions in membrane scission
946 in clathrin-independent endocytosis. *Nature* 517: 493-496
947 Richards DA, Rizzoli SO, Betz WJ (2004) Effects of wortmannin and latrunculin A on slow
948 endocytosis at the frog neuromuscular junction. *J Physiol* 557: 77-91
949 Ritter B, Ferguson SM, De Camilli P, McPherson PS (2017) A lentiviral system for efficient
950 knockdown of proteins in neuronal cultures [version 1; referees: 2 approved]. *MNI Open Res* 1
951 Roux A, Uyhazi K, Frost A, De Camilli P (2006) GTP-dependent twisting of dynamin implicates
952 constriction and tension in membrane fission. *Nature* 441: 528-531
953 Saffarian S, Cocucci E, Kirchhausen T (2009) Distinct dynamics of endocytic clathrin-coated pits
954 and coated plaques. *PLoS Biol* 7: e1000191
955 Saheki Y, De Camilli P (2012) Synaptic vesicle endocytosis. *Cold Spring Harbor perspectives in*
956 *biology* 4: a005645
957 Sakaba T, Kononenko NL, Bacetic J, Pechstein A, Schmoranzer J, Yao L, Barth H, Shupliakov O,
958 Kobler O, Aktories K *et al* (2013) Fast neurotransmitter release regulated by the endocytic scaffold
959 intersectin. *Proc Natl Acad Sci U S A* 110: 8266-8271

960 Sakaba T, Neher E (2003) Involvement of actin polymerization in vesicle recruitment at the calyx
961 of Held synapse. *J Neurosci* 23: 837-846
962 Sankaranarayanan S, Atluri PP, Ryan TA (2003) Actin has a molecular scaffolding, not propulsive,
963 role in presynaptic function. *Nat Neurosci* 6: 127-135
964 Schmied C, Soykan T, Bolz S, Haucke V, Lehmann M (2021) SynActJ: Easy-to-Use Automated
965 Analysis of Synaptic Activity. *Front Comp Sci-Switz* 3
966 Shinohara R, Thumkeo D, Kamijo H, Kaneko N, Sawamoto K, Watanabe K, Takebayashi H,
967 Kiyonari H, Ishizaki T, Furuyashiki T *et al* (2012) A role for mDia, a Rho-regulated actin
968 nucleator, in tangential migration of interneuron precursors. *Nat Neurosci* 15: 373-380, S371-372
969 Shupliakov O, Bloom O, Gustafsson JS, Kjaerulff O, Low P, Tomilin N, Pieribone VA, Greengard
970 P, Brodin L (2002) Impaired recycling of synaptic vesicles after acute perturbation of the
971 presynaptic actin cytoskeleton. *Proc Natl Acad Sci U S A* 99: 14476-14481
972 Soykan T, Kaempf N, Sakaba T, Vollweiter D, Goerdeler F, Puchkov D, Kononenko NL, Haucke
973 V (2017) Synaptic Vesicle Endocytosis Occurs on Multiple Timescales and Is Mediated by
974 Formin-Dependent Actin Assembly. *Neuron* 93: 854-866 e854
975 Soykan T, Maritzen T, Haucke V (2016) Modes and mechanisms of synaptic vesicle recycling.
976 *Curr Opin Neurobiol* 39: 17-23
977 Watanabe S, Boucrot E (2017) Fast and ultrafast endocytosis. *Curr Opin Cell Biol* 47: 64-71
978 Watanabe S, Rost BR, Camacho-Perez M, Davis MW, Sohl-Kielczynski B, Rosenmund C,
979 Jorgensen EM (2013) Ultrafast endocytosis at mouse hippocampal synapses. *Nature* 504: 242-247
980 Watanabe S, Trimbuch T, Camacho-Perez M, Rost BR, Brokowski B, Sohl-Kielczynski B, Felies
981 A, Davis MW, Rosenmund C, Jorgensen EM (2014) Clathrin regenerates synaptic vesicles from
982 endosomes. *Nature* 515: 228-233

983 Willems J, de Jong APH, Scheefhals N, Mertens E, Catsburg LAE, Poorthuis RB, de Winter F,
984 Verhaagen J, Meye FJ, MacGillavry HD (2020) ORANGE: A CRISPR/Cas9-based genome
985 editing toolbox for epitope tagging of endogenous proteins in neurons. *PLoS Biol* 18: e3000665
986 Wu LG, Chan CY (2022) Multiple Roles of Actin in Exo- and Endocytosis. *Front Synaptic*
987 *Neurosci* 14: 841704
988 Wu XS, Lee SH, Sheng J, Zhang Z, Zhao WD, Wang D, Jin Y, Charnay P, Ervasti JM, Wu LG
989 (2016) Actin Is Crucial for All Kinetically Distinguishable Forms of Endocytosis at Synapses.
990 *Neuron*
991 Wu Y, O'Toole ET, Girard M, Ritter B, Messa M, Liu X, McPherson PS, Ferguson SM, De Camilli
992 P (2014) A dynamin 1-, dynamin 3- and clathrin-independent pathway of synaptic vesicle
993 recycling mediated by bulk endocytosis. *Elife* 3: e01621
994 Xu Y, Moseley JB, Sagot I, Poy F, Pellman D, Goode BL, Eck MJ (2004) Crystal structures of a
995 Formin Homology-2 domain reveal a tethered dimer architecture. *Cell* 116: 711-723
996 Zhou L, McInnes J, Wierda K, Holt M, Herrmann AG, Jackson RJ, Wang YC, Swerts J, Beyens
997 J, Miskiewicz K *et al* (2017) Tau association with synaptic vesicles causes presynaptic
998 dysfunction. *Nat Commun* 8: 15295
999
1000

1001 **FIGURES**

Figure 1

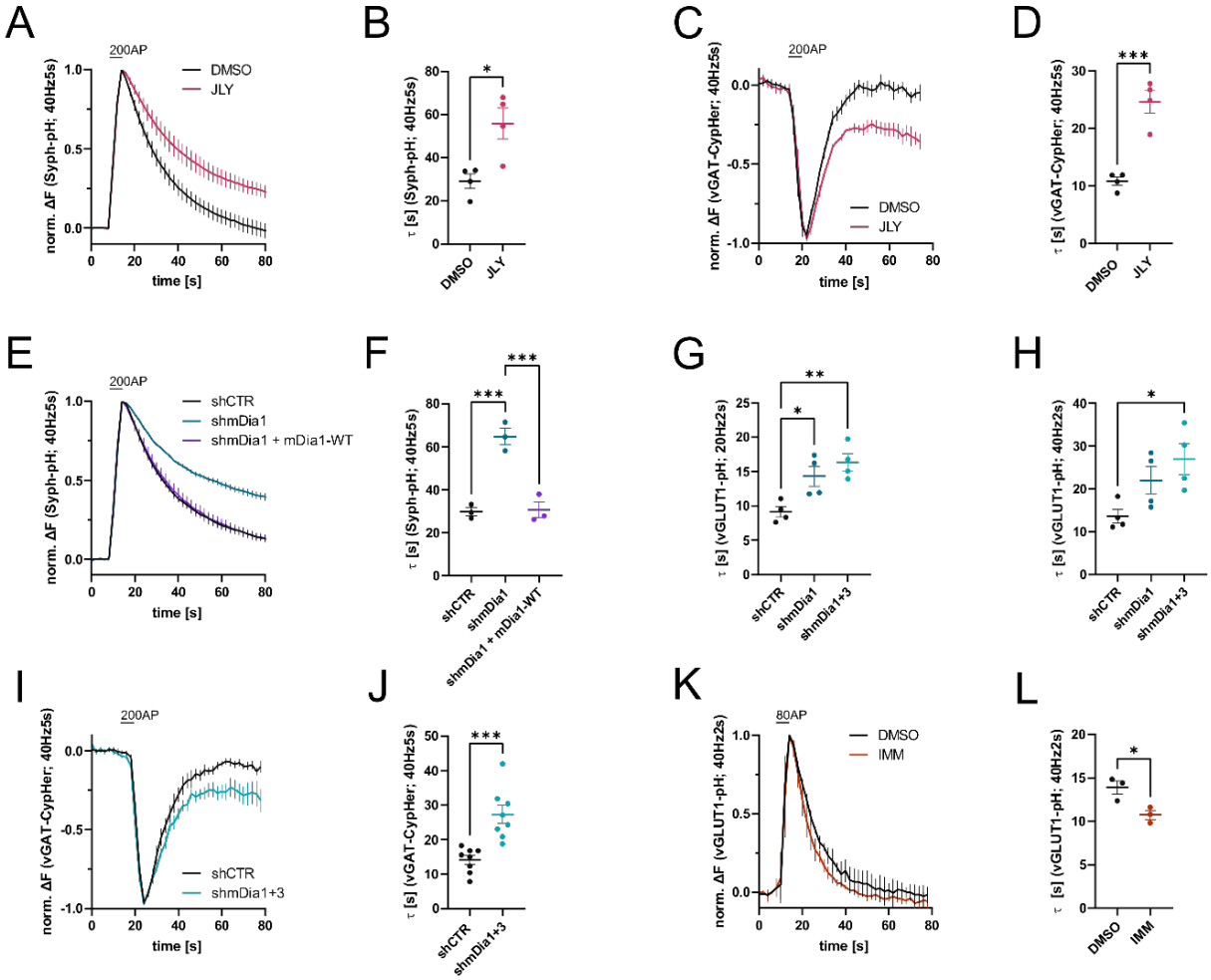

1002

1003 **Figure 1 | Actin dynamics and actin-nucleating mDia1/3 proteins facilitate SV endocytosis.**

1004 **(A)** Averaged normalized Synaptophysin-pHluorin (Syph-pH) fluorescence traces from

1005 transfected hippocampal neurons stimulated with 200 APs (40 Hz, 5s) at physiological temperature

1006 (37.5°C). Neurons were treated with 0.1% DMSO or JLY cocktail (containing 8 µM

1007 Jasplakinolide, 5 µM Latrunculin A and 10 µM Y-27632) as indicated. Data shown represent the

1008 mean ± SEM. N = 4 independent experiments from n_{DMSO} = 23 videos; n_{JLY} = 36videos.

1009 **(B)** Endocytic decay constants (τ) of Synaptophysin-pHluorin traces in A: τ_{DMSO} = 29.1 ± 3.4 s;

1010 τ_{JLY} = 55.8 ± 7.2 s; $p < 0.05$, two-tailed student's t-test. Data shown represent mean ± SEM.

1011 **(C)** Averaged normalized bleach-corrected vGAT-CypHer fluorescence traces from hippocampal
1012 neurons treated with DMSO or JLY cocktail in response to 200 AP (40 Hz, 5s) stimulation. Data
1013 shown represent the mean ± SEM. N = 4 independent experiments from n_{DMSO} = 23 videos; n_{JLY}
1014 = 29 videos.
1015 **(D)** Endocytic decay constants of vGAT-CypHer traces in C: τ_{DMSO} = 10.9 ± 0.7 s, τ_{JLY} = 24.6 ±
1016 2.0 s; $p < 0.001$, two-tailed unpaired student's t-test. Data shown represent the mean ± SEM.
1017 **(E)** Averaged normalized Synaptophysin-pHluorin fluorescence traces from hippocampal neurons
1018 transfected with shRNA-encoding plasmids against no mammalian target (shCTR) or mDia1
1019 (shmDia1) in response to 200 AP (40 Hz, 5s) stimulation. Neurons were co-transfected with
1020 mDia1-mCherry (mDia1-WT) or mCherry alone (shCTR & shmDia1) to exclude artefacts from
1021 overexpression. Data shown represent the mean ± SEM. N = 3 independent experiments from
1022 n_{shCTR} = 28 videos, $n_{shmDia1}$ = 21 videos, $n_{shmDia1 + mDia1\text{-}WT}$ = 21 videos.
1023 **(F)** Endocytic decay constants of Synaptophysin-pHluorin traces in E: τ_{shCTR} = 29.7 ± 1.9 s;
1024 $\tau_{shmDia1}$ = 64.7 ± 3.9 s; $\tau_{shmDia1 + mDia1\text{-}WT}$ = 30.6 ± 3.7 s; $p_{shCTR\ vs\ shmDia1} < 0.001$, $p_{shmDia1\ vs\ shmDia1 +}$
1025 $_{mDia1\text{-}WT} < 0.001$, one-way ANOVA with Tukey's post-test. Data shown represent mean ± SEM.
1026 **(G)** Endocytic decay constants of averaged normalized vGLUT1-pHluorin fluorescence traces
1027 (Figure 1 – figure supplement 1B) from hippocampal neurons transduced with shCTR (τ_{shCTR} =
1028 9.1 ± 0.8 s), shmDia1 ($\tau_{shmDia1}$ = 14.3 ± 1.5 s) or shmDia1+3 ($\tau_{shmDia1+3}$ = 16.4 ± 1.3 s) in response
1029 to 40 AP (20 Hz, 2s) stimulation ($p_{shCTR\ vs\ shmDia1} < 0.05$, $p_{shCTR\ vs\ shmDia1+3} < 0.01$, one-way ANOVA
1030 with Tukey's post-test). Data shown represent mean ± SEM. N = 4 independent experiments from
1031 n_{shCTR} = 17 videos; $n_{shmDia1}$ = 19 videos; $n_{shmDia1+3}$ = 18 videos.
1032 **(H)** Endocytic decay constants of averaged normalized vGLUT1-pHluorin fluorescence traces
1033 (Figure 1 – figure supplement 1C) of neurons transduced with lentiviral vectors encoding shCTR
1034 (τ_{shCTR} = 13.6 ± 1.6 s), shmDia1 ($\tau_{shmDia1}$ = 22.0 ± 3.2 s) or shmDia1+3 ($\tau_{shmDia1+3}$ = 26.9 ± 3.6 s)

1035 in response to 80 AP (40 Hz, 2s) stimulation ($p_{shCTR\ vs\ shmDia1+3} < 0.05$, one-way ANOVA with
1036 Tukey's post-test). Data shown represent mean ± SEM. N = 4 independent experiments from n_{shCTR}
1037 = 12 videos, $n_{shmDia1}$ = 15 videos, $n_{shmDia1+3}$ = 18 videos.
1038 **(I)** Averaged normalized bleach-corrected vGAT-CypHer fluorescence traces from hippocampal
1039 neurons transduced with shCTR or shmDia1+3 in response to 200 AP (40 Hz, 5s) stimulation.
1040 Data shown represent the mean ± SEM. N = 8 independent experiments from n_{shCTR} = 37 videos,
1041 $n_{shmDia1+3}$ = 35 videos.
1042 **(J)** Endocytic decay constants of vGAT-CypHer traces in I: τ_{shCTR} = 14.1 ± 1.3 s; $\tau_{shmDia1+3}$ = 27.3
1043 ± 2.6 s; $p < 0.001$, two-tailed unpaired student's t-test. Data shown represent the mean ± SEM.
1044 **(K)** Averaged normalized vGLUT1-pHluorin fluorescence traces from transduced neurons in
1045 response to 80 AP (40 Hz, 2s) stimulation. Cells were treated with 0.1% DMSO or 10 µM mDia
1046 activator (IMM) in the imaging buffer. Data shown represent mean ± SEM. N = 3 independent
1047 experiments from n_{DMSO} = 18 videos; n_{IMM} = 16 videos.
1048 **(L)** Endocytic decay constants of vGLUT1-pHluorin traces in K: τ_{DMSO} = 14.9 ± 0.8 s; τ_{IMM}= 9.8
1049 ± 0.5 s; $p < 0.05$, two-tailed unpaired student's t-test. Data shown represent mean ± SEM.
1050

Figure 2

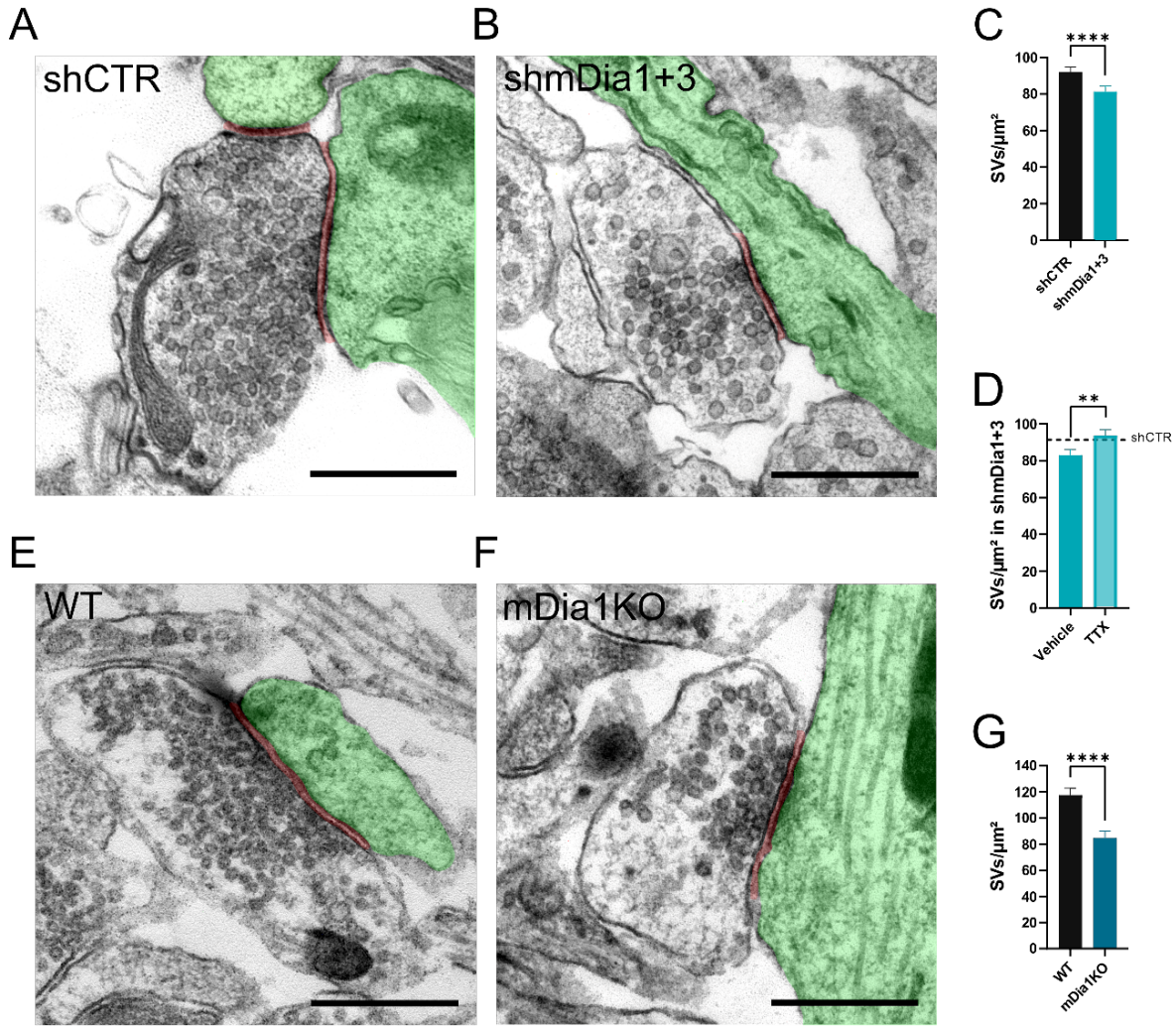

Figure 2 | Loss of mDia1/3 causes an activity-dependent reduction of the SV pool.

(A,B) Representative synaptic electron micrographs from hippocampal neurons transduced with lentiviruses encoding shCTR (A) or shmDia1+3 (B). Postsynapse and postsynaptic cleft are colored in green and maroon, respectively. Scale bar, 250 nm.

(C) Average number of SVs per μm^2 in boutons from shCTR (92.2 ± 2.5) and shmDia1+3 (81.4 ± 2.9; $p < 0.0001$, Mann-Whitney test) treated neurons. Data shown represent mean ± SEM. N = 3 independent experiments from n_{shCTR} = 326 synapses, $n_{shmDia1+3}$ = 321 synapses.

1059 **(D)** Average number of SVs per μm^2 in synaptic boutons from hippocampal neurons transduced
1060 with lentiviruses encoding shmDia1+3 and treated with 0.1 % Vehicle (10 µM NaOAc; 83.2 ±
1061 2.9) or 1 µM Tetrodotoxin (TTX; 93.8 ± 3.1; $p < 0.01$, Mann-Whitney test) for 36 h before
1062 chemical fixation. Data shown represent mean ± SEM from two independent experiments and
1063 $n_{Vehicle} = 225$ synapses, $n_{TTX} = 221$ synapses. Representative synaptic electron micrographs are
1064 shown in figure 2 – figure supplement 1D, E. The dotted line represents the average SV numbers/
1065 μm^2 in shCTR boutons treated with DMSO from the same experiments as a reference (see figure
1066 2 – figure supplement 1A-C).
1067 **(E,F)** Representative electron micrographs of synapses in hippocampal neurons from WT (E) or
1068 mDia1 KO mice (F). Postsynapse and postsynaptic cleft are colored in green and maroon,
1069 respectively. Scale bar, 250nm.
1070 **(G)** Average number of SVs per μm^2 in WT (117.6 ± 5.3) and mDia1 KO (84.6 ± 5.2; $p < 0.0001$,
1071 Mann-Whitney test) boutons. Data shown represent the mean ± SEM from $n_{WT} = 103$, $n_{KO} = 96$
1072 synapses.
1073
1074

Figure 3

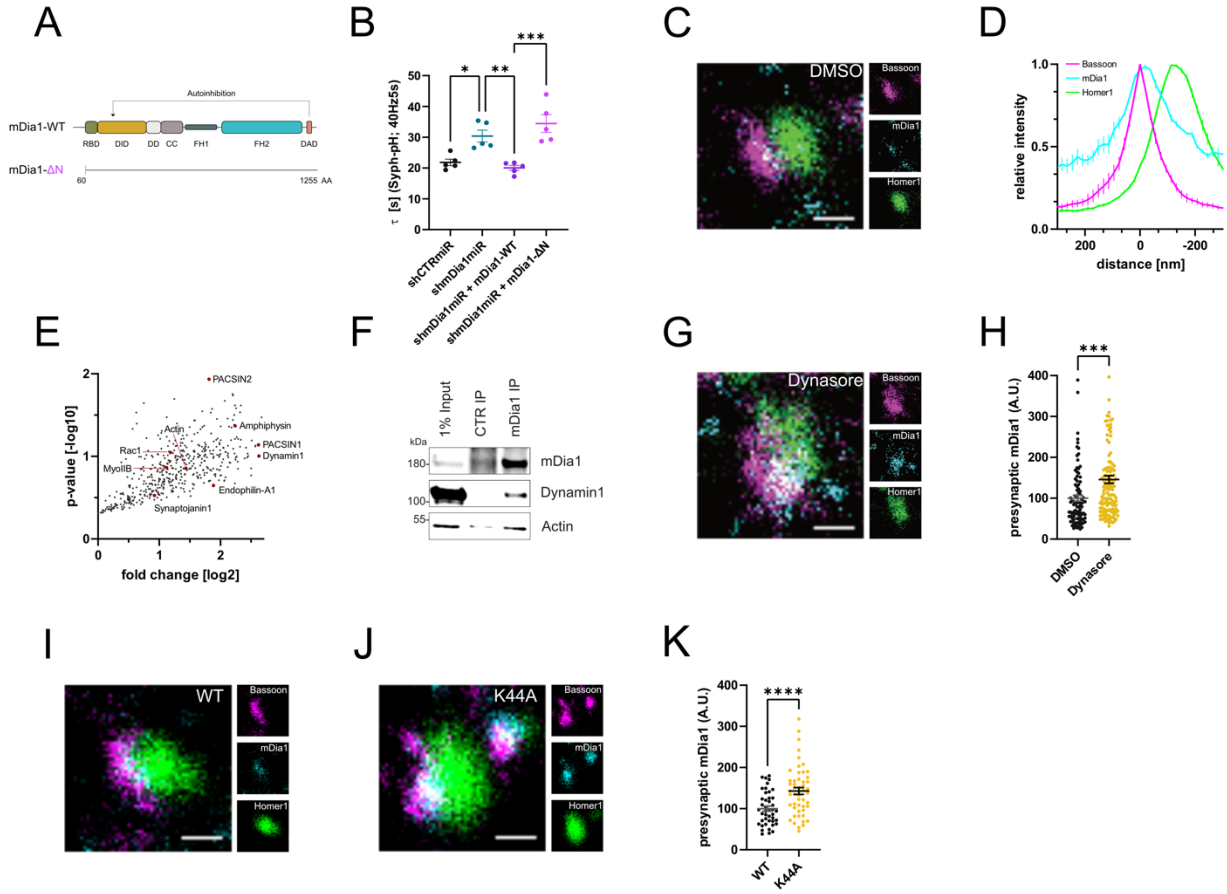

Figure 3 | mDia1 associates with endocytic proteins and localizes to presynaptic sites.

(A) Schematic representation of functional domains of mDia1. Rho-binding domain (RBD), Diaphanous inhibitory domain (DID), Dimerization domain (DD), Coiled coil domain (CC), Formin homology domain 1 (FH1), Formin homology domain 2 (FH2), Diaphanous autoinhibitory domain (DAD). The unstructured N-terminus (first 60 amino acids) contains three basic stretches and was truncated in the ΔN mutant.

(B) Endocytic decay constants of Synaptophysin-pHluorin traces (see Figure 2- supplement 1C) from hippocampal neurons transfected with shRNAmiR against no mammalian target (shCTRmiR) or mDia1 (shmDia1miR) in response to 200 AP (40 Hz, 5s) stimulation. For rescue experiments, neurons were co-transfected with plasmids encoding mDia1-WT-mCherry

1086 ($\tau_{shmDia1miR + mDia1\text{-}WT}$ = 20.0 ± 0.8 s), mDia1-ΔN-mCherry ($\tau_{shmDia1miR + mDia1\text{-}\Delta N}$ = 34.5 ± 2.9 s) or
1087 mCherry alone ($\tau_{shCTRmiR}$ = 21.8 ± 1.1 s, $\tau_{shmDia1miR}$ = 30.4 ± 1.9 s) to exclude artefacts from
1088 overexpression ($p_{shCTRmiR\ vs\ shmDia1miR} < 0.05$; $p_{shmDia1miR\ vs\ shmDia1miR + mDia1\text{-}WT} < 0.01$; $p_{shmDia1miR +}$
1089 $_{mDia1\text{-}WT\ vs\ shmDia1miR + mDia1\text{-}\Delta N} < 0.01$, one-way ANOVA with Tukey's post-test). Data shown
1090 represent mean ± SEM. N = 5 independent experiments from $n_{shCTRmiR}$ = 41 videos, $n_{shmDia1miR}$ =
1091 51 videos, $n_{shmDia1miR + mDia1\text{-}WT}$ = 35 videos, $n_{shmDia1miR + mDia1\text{-}\Delta N}$ = 37 videos.
1092 **(C)** Representative three-channel time-gated STED image of a synapse from hippocampal cultures
1093 treated with 0.1% DMSO for 10 min before fixation and immunostained for Bassoon (presynaptic
1094 marker, magenta), mDia1 (cyan) and Homer1 (postsynaptic marker, green). Scale bar, 250 nm.
1095 **(D)** Averaged normalized line profiles for synaptic distribution of mDia1 and Homer1 relative to
1096 Bassoon (Maximum set to 0 nm). Data represent mean ± SEM. N = 3 independent experiments
1097 from n = 235 synapses.
1098 **(E)** Volcano plot of proteins associating with synaptic mDia1 analyzed by label-free proteomics
1099 of anti-mDia1 versus control (CTR) immunoprecipitates from detergent-extracted mouse
1100 synaptosomes (P2' fraction). The logarithmic ratios of protein intensities are plotted against
1101 negative logarithmic p-values derived from two-tailed student's t-test. N = 3 independent
1102 experiments. Each dot represents one protein/gene. Selected cytoskeletal hits include: Actin,
1103 Myosin IIB (MyoIIB) and Rac1. Selected endocytic hits include Amphiphysin ($p < 0.05$),
1104 Dynamin1, Endophilin-A1, PACSIN1, PACSIN2 ($p < 0.05$) and Synaptojanin1.
1105 **(F)** Endogenous immunoprecipitation of mDia1 from detergent-extracted mouse synaptosomes
1106 (P2' fraction) using mDia1-specific antibodies. Immunoprecipitates were analyzed by
1107 immunoblotting for mDia1, Dynamin1 and β-Actin.
1108 **(G)** Representative three-channel time-gated STED image of a synapse from hippocampal
1109 cultures, treated with 80 μM Dynasore for 10 min before fixation and immunostained for Bassoon

1110 (magenta), mDia1 (cyan) and Homer1 (green). Images C and G stem from the same experiment
1111 and brightness and contrast of all three channels were set to the same values. Scale bar, 250 nm.
1112 **(H)** Presynaptic mDia1 levels in synapses treated with 0.1% DMSO (100 ± 7.3) or 80 µM
1113 Dynasore (145.8 ± 9.3; $p = 0.0001$; one sample Wilcoxon test) for 10 min in response to 200 AP
1114 (40 Hz, 5s) stimulation. Absolute line profiles of mDia1 overlapping with Bassoon (presynapse)
1115 distribution were integrated. Data shown are normalized to DMSO (set to 100) and expressed as
1116 mean ± SEM. N = 3 independent experiments from $n_{DMSO} = 92$ synapses, $n_{Dynasore} = 135$ synapses.
1117 **(I,J)** Representative three-channel time-gated STED images of synapses from hippocampal
1118 cultures transduced with wildtype Dynamin1 (WT; I) or GTPase-deficient Dynamin1 (K44A; J)
1119 in response to 200 AP (40 Hz, 5s) stimulation. Cells were immunostained for Bassoon (magenta),
1120 mDia1 (cyan) and Homer1 (green). Scale bar, 250 nm.
1121 **(K)** Presynaptic mDia1 levels in synapses from hippocampal neurons transduced with wildtype
1122 Dynamin1 (WT; 100 ± 6.2) or GTPase-deficient Dynamin1 (K44A; 142.9 ± 8.3, $p < 0.0001$, one
1123 sample Wilcoxon test) in response to 200 AP (40 Hz, 5s) stimulation. Line profiles of mDia1
1124 overlapping with Bassoon distribution were integrated. Data shown are normalized to Dynamin1-
1125 WT (set to 100) and expressed as mean ± SEM. N = 2 independent experiments from $n_{WT} = 43$
1126 synapses, $n_{K44A} = 51$ synapses.
1127

Figure 4

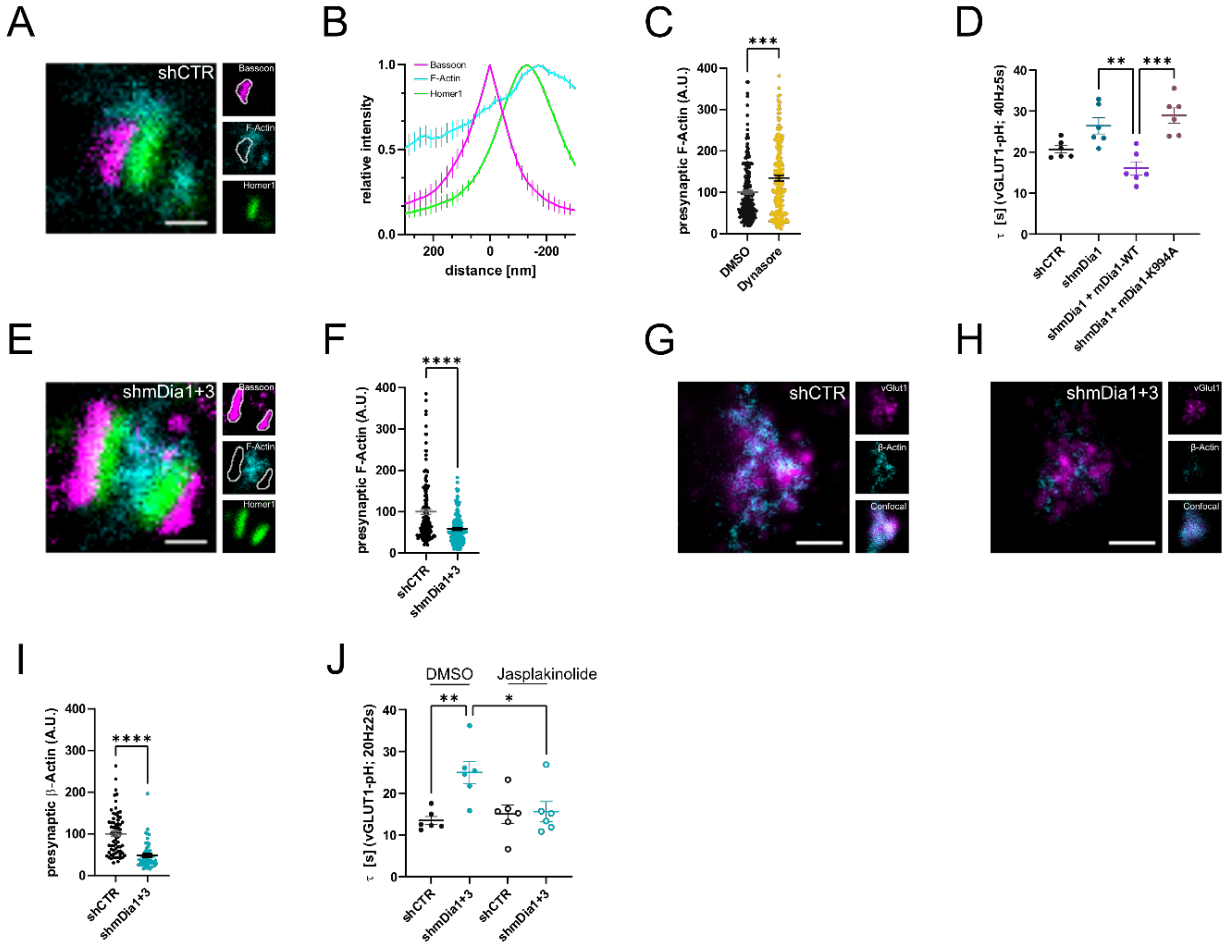

Figure 4 | mDia facilitates SV endocytosis by regulating presynaptic F-actin.

(A) Representative three-channel time-gated STED image of a synapse from hippocampal cultures transduced with shCTR, fixed and immunostained for Bassoon (presynaptic marker, magenta), F-Actin (cyan) and Homer1 (postsynaptic marker, green). Scale bar, 250 nm.

(B) Averaged normalized line profiles for synaptic distribution of F-Actin and Homer1 relative to Bassoon (Maximum set to 0 nm). Data are expressed as mean ± SEM. N = 4 independent experiments from n = 154 synapses.

(C) Presynaptic F-Actin levels in synapses treated with 0.1% DMSO (Figure 4 – figure supplement 1A; 100 ± 4.8) or 80 µM Dynasore (Figure 4 – figure supplement 1B; 134.7 ± 6.8; p = 0.001, one

1138 sample Wilcoxon test) for 10 min before fixation. Cells were immunostained for Bassoon
1139 (magenta), F-Actin (cyan), and Homer1 (green). Absolute line profiles of F-Actin overlapping
1140 with Bassoon (presynapse) distribution were integrated. Data shown are normalized to DMSO (set
1141 to 100) and expressed as mean ± SEM. N = 3 independent experiments from n_{DMSO} = 207 synapses,
1142 $n_{Dynasore}$ = 211 synapses.

1143 **(D)** Endocytic decay constants of vGLUT1-pHluorin traces from hippocampal neurons transduced
1144 with lentiviral particles encoding shCTR (τ_{shCTR} = 20.7 ± 0.9 s) or shmDia1 ($\tau_{shmDia1}$ = 26.4 ± 2.0
1145 s) in response to 200 AP (40 Hz, 5s) stimulation. For rescue experiments, neurons were co-
1146 transduced with lentiviruses encoding mDia1-WT-SNAP ($\tau_{shmDia1 + mDia1\text{-}WT}$ = 16.1 ± 1.9 s) or
1147 mDia1-K994A-SNAP ($\tau_{shmDia1 + mDia1\text{-}K994A}$ = 29.0 ± 1.9 s) ($p_{shmDia1 \text{ vs } shmDia1 + mDia1\text{-}WT}$ < 0.01;
1148 $p_{shmDia1 + mDia1\text{-}WT \text{ vs } shmDia1 + mDia1\text{-}K994A}$ < 0.001, one-way ANOVA with Tukey's post-test). Data are
1149 expressed as mean ± SEM. N = 6 independent experiments from n_{shCTR} = 21 videos; $n_{shmDia1}$ =
1150 21 videos, $n_{shmDia1 + mDia1\text{-}WT}$ = 16 videos, $n_{shmDia1 + mDia1\text{-}K994A}$ = 19 videos.

1151 **(E)** Representative three-channel time-gated STED image of two synapses from hippocampal
1152 cultures, transduced with shmDia1+3, fixed and immunostained for Bassoon (magenta), F-Actin
1153 (cyan) and Homer1 (green). Synapses from A and E stem from the same experiment and brightness
1154 and contrast of all three channels were set to the same values. Scale bar, 250 nm.

1155 **(F)** Presynaptic F-Actin levels in synapses from hippocampal cultures transduced with shCTR (A;
1156 100 ± 6.4) or shmDia1+3 (E; 58.1 ± 2.9; p < 0.001, one sample Wilcoxon test). Line profiles of F-
1157 Actin overlapping with Bassoon (presynapse) distribution were integrated. Data shown are
1158 normalized to shCTR (set to 100) and expressed as mean ± SEM. N = 4 independent experiments
1159 from n_{shCTR} = 155 synapses, $n_{shmDia1+3}$ = 158 synapses.

1160 **(G,H)** Representative confocal and two-channel time-gated STED images of endogenous β-Actin
1161 (cyan) in vGLUT1 (magenta) positive boutons from hippocampal neurons transduced with

1162 lentiviruses encoding shCTR (G) or shmDia1+3 (H). Synapses from G and H stem from the same
1163 experiment and brightness and contrast of the β-Actin channel were set to the same values. Scale
1164 bar, 250 nm.
1165 **(I)** Analysis of presynaptic endogenous β-Actin levels in vGLUT1 positive boutons from shCTR
1166 (G; 100 ± 6.3) and shmDia1+3 (H; 47.7 ± 4.3; $p < 0.0001$ one sample Wilcoxon test) transduced
1167 neurons. β-Actin STED mean intensity was measured using confocal vGLUT1 signal as a mask.
1168 Data shown are normalized to shCTR (set to 100) and expressed as mean ± SEM from two
1169 independent experiments and $n_{shCTR} = 67$ synapses, $n_{shmDia1+3} = 53$ synapses.
1170 **(J)** Endocytic decay constants of vGLUT1-pHluorin traces (Figure 4 – figure supplement 1I) for
1171 neurons transduced with shCTR or shmDia1+3 in response to 40 AP (20 Hz, 2s) stimulation.
1172 Neurons were pre-incubated with 0.1 % DMSO or 1 μM Jasplakinolide (Jasp) for 30 min in the
1173 media before imaging ($\tau_{shCTR + DMSO} = 13.4 \pm 1.0$ s, $\tau_{shCTR + Jasp} = 15.0 \pm 2.2$ s, $\tau_{shmDia1+3 + DMSO} =$
1174 25.0 ± 2.7 s, $\tau_{shmDia1+3 + Jasp} = 15.6 \pm 2.4$ s; $p_{shCTR\ vs\ shmDia1+3} < 0.01$; $p_{shmDia1+3 + DMSO\ vs\ shmDia1+3 + Jasp}$
1175 < 0.05, one-way ANOVA with Tukey's post-test). Data are expressed as mean ± SEM. N = 6
1176 independent experiments from $n_{shCTR + DMSO} = 32$ videos, $n_{shmDia1+3 + DMSO} = 35$ videos, $n_{shCTR + Jasp}$
1177 $= 33$ videos; $n_{shmDia1+3 + Jasp} = 34$ videos).
1178
1179

Figure 5

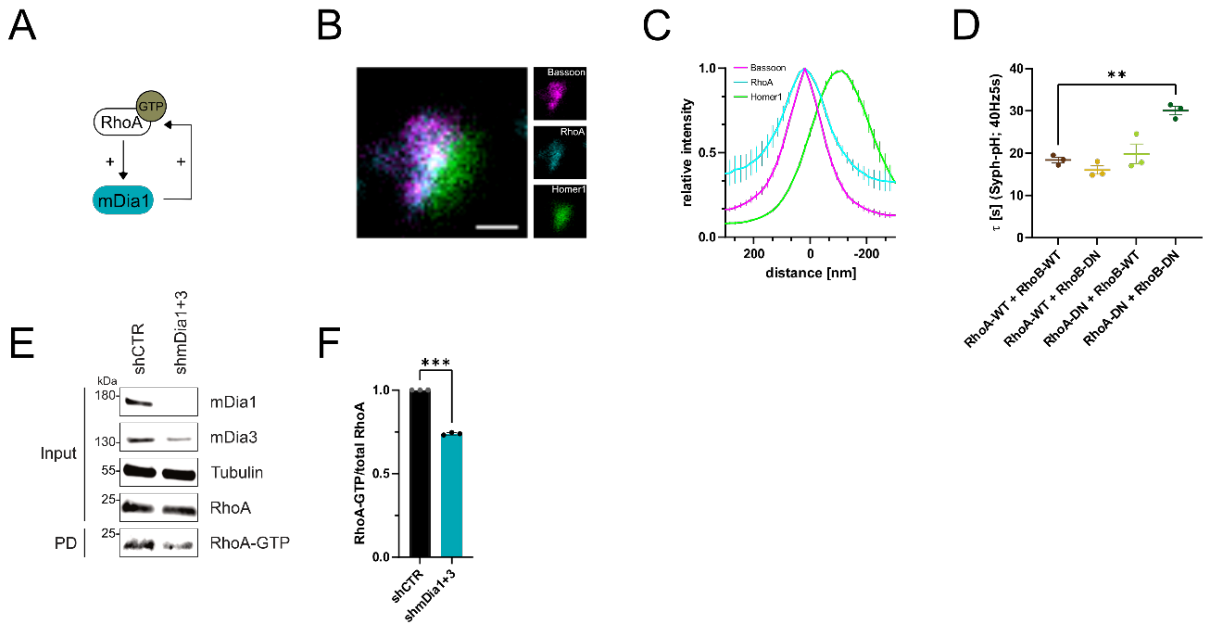

Figure 5 | RhoA/B facilitate presynaptic endocytosis and are regulated by mDia1/3.

(A) Schematic representation of activation of mDia1 by RhoA-GTP and positive feedback loop of mDia1 on RhoA-GTP levels through GEF stimulation.

(B) Representative three-channel time-gated STED image of a synapses from hippocampal cultures, fixed and immunostained for Bassoon (magenta), RhoA (cyan) and Homer1 (green). Scale bar, 250 nm.

(C) Averaged normalized line profiles for synaptic distribution of RhoA and Homer1 relative to Bassoon (Maximum set to 0 nm). Data are expressed as mean ± SEM. N = 5 independent experiments from n = 230 synapses.

(D) Endocytic decay constants of averaged normalized Synaptophysin-pHluorin fluorescence traces (figure5 – figure supplement 1A) in response to 200 AP (40 Hz, 5s) stimulation. Neurons were transfected with the annotated combinations of plasmids encoding wild-type (WT) or dominant-negative (DN, T19N mutation) RhoA and RhoB ($\tau_{RhoA\text{-}WT + RhoB\text{-}WT}$ = 18.4 ± 0.7 s, $\tau_{RhoA\text{-}}$

1194 $_{WT + RhoB\text{-}DN}$ = 16.0 ± 1.0 s, $\tau_{RhoA\text{-}DN + RhoB\text{-}WT}$ = 19.8 ± 2.4 s, $\tau_{RhoA\text{-}DN + RhoB\text{-}DN}$ = 30.1 ± 1.0 s; $p_{RhoA\text{-}}$

1195 $_{WT + RhoB\text{-}WT \text{ vs } RhoA\text{-}DN + RhoB\text{-}DN}$ < 0.01, one-way ANOVA with Tukey's post-test). Data shown

1196 represent mean ± SEM. N = 3 independent experiments from $n_{RhoA\text{-}WT + RhoB\text{-}WT}$ = 21 videos, $n_{RhoA\text{-}}$

1197 $_{DN + RhoB\text{-}WT}$ = 31 videos, $n_{RhoA\text{-}WT + RhoB\text{-}DN}$ = 23 videos, $n_{RhoA\text{-}DN + RhoB\text{-}DN}$ = 22 videos.

1198 **(E)** Analysis of RhoA activity by RhoA-GTP pulldown (PD) from whole-cell lysates (input) of

1199 mouse hippocampal neurons expressing shCTR or shmDia1+3 using immobilized Rhotekin as a

1200 bait. Samples were analyzed by immunoblotting for mDia1, mDia3, RhoA and Tubulin using

1201 specific antibodies. Input, 10% of material used for the pulldown. Contrast of pulldown and input

1202 blots was seperatly adjusted for visualisation purposes.

1203 **(F)** Densitometric quantification of RhoA-GTP normalized to total RhoA levels (input) in lysates

1204 from neurons transduced with shCTR or shmDia1+3 (0.7 ± 0.0, $p < 0.001$, one sample t-test) from

1205 immunoblots exemplified in E. Values for shCTR were set to 1. Data are expressed as mean ±

1206 SEM from N = 3 independent experiments.

1207

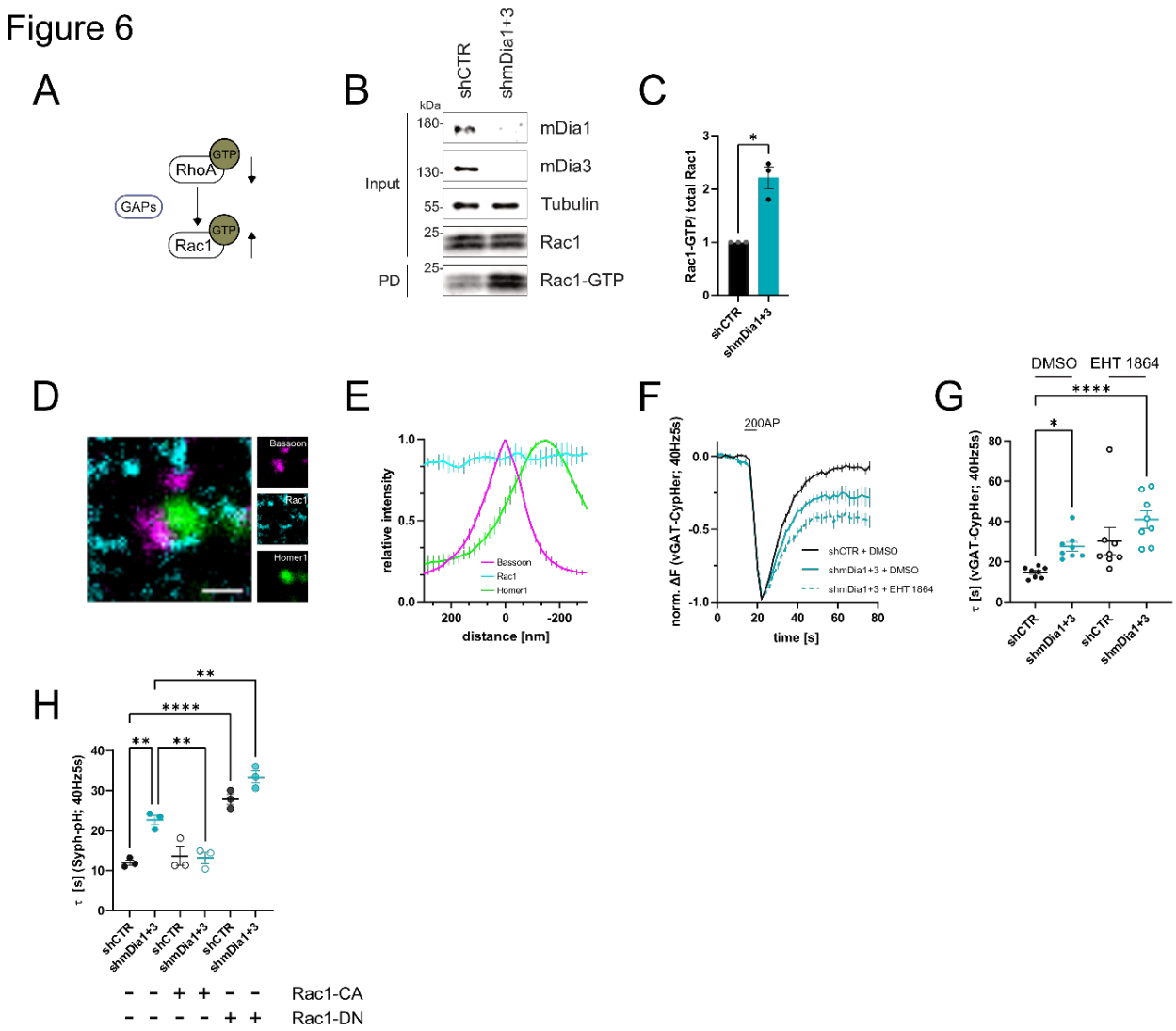

Figure 6 | mDia1/3-Rho and Rac1 signaling facilitates presynaptic endocytosis.

(A) Schematic of the interplay between RhoA and Rac1 signaling via GTPase activating proteins (GAPs) common for RhoA and Rac1.

(B) Analysis of Rac1 activity by Rac1-GTP pulldown (PD) from whole-cell lysates (input) of mouse hippocampal neurons expressing shCTR or shmDia1+3 utilizing immobilized PAK as a bait. Samples were analyzed by immunoblotting for mDia1, mDia3, Rac1 and Tubulin using specific antibodies. Input, 10% of material used for the pulldown. Contrast of pulldown and input blots was seperatly adjusted for visualisation purposes.

1217 **(C)** Densitometric quantification of Rac1-GTP normalized to total Rac1 levels (input) in lysates
1218 from neurons transduced with shCTR or shmDia1+3 (2.2 ± 0.2; $p < 0.05$, one sample t-test) from
1219 immunoblots exemplified in (B). Values for shCTR were set to 1. Data are expressed as mean ±
1220 SEM from N = 3 independent experiments.
1221 **(D)** Representative three-channel time-gated STED image of a synapses from hippocampal
1222 cultures, fixed and immunostained for Bassoon (magenta), Rac1 (cyan) and Homer1 (green). Scale
1223 bar, 250 nm.
1224 **(E)** Averaged normalized line profiles for synaptic distribution of Rac1 and Homer1 relative to
1225 Bassoon (Maximum set to 0 nm). Data represent mean ± SEM. N = 3 independent experiments
1226 from n = 79 synapses.
1227 **(F)** Averaged normalized vGAT-CypHer fluorescence traces for neurons transduced with shCTR
1228 or shmDia1+3 in response to 200 AP (40 Hz, 5 s) stimulation. Cells were acutely treated with
1229 0.1 % DMSO or 10 µM Rac1 Inhibitor (EHT 1864) in the imaging buffer. Data shown represent
1230 the mean ± SEM. N = 8 independent experiments from $n_{shCTR + DMSO}$ = 46 videos, $n_{shmDia1+3 + DMSO}$
1231 = 45 videos, $n_{shCTR + EHT\ 1864}$ = 42 videos, $n_{shmDia1+3 + EHT\ 1864}$ = 43 videos.
1232 **(G)** Endocytic decay constants of vGAT-CypHer traces in F: $\tau_{shCTR + DMSO}$ = 14.7 ± 0.9 s, $\tau_{shmDia1+3}$
1233 $_{+ DMSO}$ = 27.5 ± 2.3 s, $\tau_{shCTR + EHT\ 1864}$ = 30.3 ± 6.7 s, $\tau_{shmDia1+3 + EHT\ 1864}$ = 41.0 ± 4.3 s; $p_{shCTR + DMSO}$
1234 $_{vs\ shmDia1+3 + DMSO}$ < 0.05, $p_{shCTR + DMSO\ vs\ shmDia1+3 + EHT\ 1864}$ < 0.0001, Kruskal-Wallis test with Dunn's
1235 post-test. Data represent mean ± SEM.
1236 **(H)** Endocytic decay constants of Synaptophysin-pHluorin traces (Figure 6 –figure supplement
1237 1K) of neurons transduced with shCTR (τ_{shCTR} = 12.0 ± 0.7 s) or shmDia1+3 ($\tau_{shmDia1+3}$ = 22.7 ±
1238 2.0 s) and transfected with constitutively active Rac1 (Rac1-CA; Q61L variant; $\tau_{shCTR + Rac1\text{-}CA}$ =
1239 13.6 ± 1.2 s, $\tau_{shmDia1+3 + Rac1\text{-}CA}$ = 13.3 ± 1.4 s) or dominant negative Rac1 (Rac1-DN; T17N variant;
1240 $\tau_{shCTR + Rac1\text{-}DN}$ = 27.8 ± 1.3 s, $\tau_{shmDia1+3 + Rac1\text{-}DN}$= 33.4 ± 1.6 s) in response to 200 AP (40 Hz, 5s)

1241 stimulation ($p_{shCTR\ vs\ shmDia1+3} < 0.01$; $p_{shCTR\ vs\ shCTR\ +\ Rac1\text{-}DN} < 0.0001$, $p_{shCTR\ vs\ shmDia1+3\ +\ Rac1\text{-}DN} <$

1242 0.01, $p_{shmDia1+3\ vs\ shmDia1+3\ +\ Rac1\text{-}DN} < 0.01$, one-way ANOVA with Tukey's post-test). Data are

1243 expressed as mean ± SEM. N = 3 independent experiments from $n_{shCTR} = 12$ videos, $n_{shmDia1+3} =$

1244 23 videos; $n_{shCTR\ +\ Rac1\text{-}CA} = 10$ videos, $n_{shmDia1+3\ +\ Rac1\text{-}CA} = 14$ videos, $n_{shCTR\ +\ Rac1\text{-}DN} = 9$ videos;

1245 $n_{shmDia1+3\ +\ Rac1\text{-}DN} = 13$ videos.

1246

1247

Figure 7

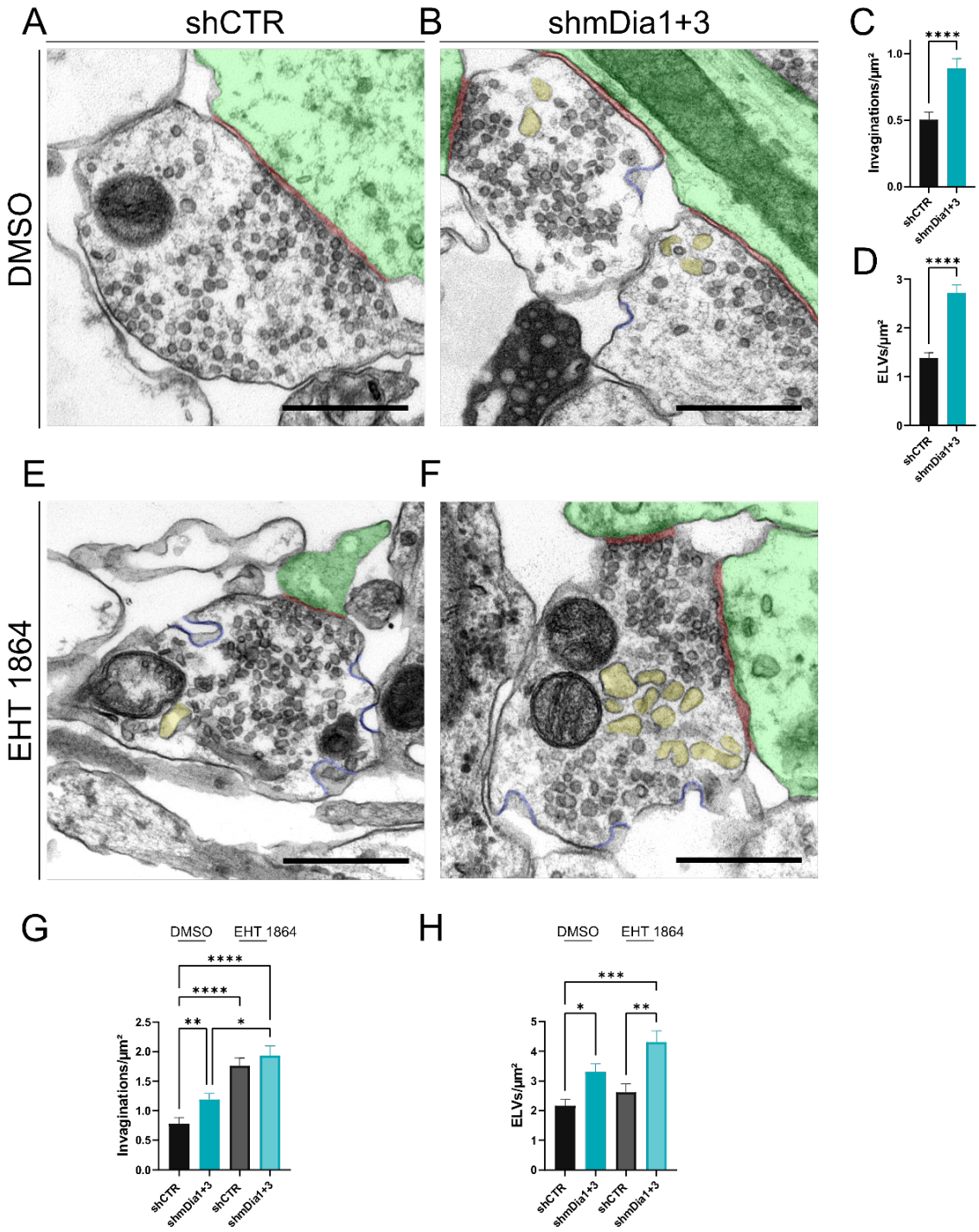

Figure 7 | Defects in presynaptic ultrastructure induced by interference with mDia1/3-Rho and Rac1 signaling.

1251 **(A,B)** Representative synaptic electron micrographs from hippocampal neurons transduced with
1252 lentiviruses encoding shCTR (A) or shmDia1+3 (B) and treated with 0.1 % DMSO before fixation.
1253 Invaginations and ELVs are colored in blue and yellow, while postsynapse and synaptic cleft are
1254 colored in green and maroon, respectively. Scale bar, 250 nm.
1255 **(C)** Average number of invaginations per μm^2 in shCTR (0.5 ± 0.1) and shmDia1+3 (0.9 ± 0.1; p
1256 < 0.0001, Mann-Whitney test) boutons. Data represent mean ± SEM. N = 3 independent
1257 experiments from $n_{shCTR} = 326$ synapses, $n_{shmDia1+3} = 323$ synapses.
1258 **(D)** Average number of ELVs per μm^2 in shCTR (1.4 ± 0.1) and shmDia1+3 (2.7 ± 0.2; $p < 0.0001$,
1259 Mann-Whitney test) boutons. Data represent mean ± SEM. N = 3 independent experiments from
1260 $n_{shCTR} = 326$ synapses, $n_{shmDia1+3} = 323$ synapses.
1261 **(E,F)** Representative synaptic electron micrographs from neurons transduced with shCTR (A) or
1262 shmDia1/3 (B) and treated with 10 µM Rac1 Inhibitor (EHT 1864) for 2 h before fixation.
1263 Invaginations and ELVs are colored in blue and yellow, while postsynapse and synaptic cleft are
1264 colored in green and maroon, respectively. Scale bar, 250nm.
1265 **(G)** Average number of invaginations per μm^2 in shCTR and shmDia1+3 boutons treated with
1266 0.1 % DMSO (0.8 ± 0.1 for shCTR; 1.2 ± 0.1 for shmDia1+3, $p_{shCTR + DMSO \text{ vs } shmDia1+3 + DMSO} <$
1267 0.01) or 10 µM EHT 1864 (1.8 ± 0.1 for shCTR, $p_{shCTR + DMSO \text{ vs } shCTR + EHT\ 1864} < 0.0001$; 1.9 ± 0.2
1268 for shmDia1+3, $p_{shCTR + DMSO \text{ vs } shmDia1+3 + EHT\ 1864} < 0.0001$, $p_{shmDia1+3 + DMSO \text{ vs } shmDia1+3 + EHT\ 1864} <$
1269 0.05, Kruskal-Wallis test with Dunn's post-test) for 2 h before fixation. Data represent mean ±
1270 SEM from $n_{shCTR + DMSO} = 144$ synapses, $n_{shmDia1+3 + DMSO} = 143$ synapses, $n_{shCTR + EHT\ 1864} = 136$
1271 synapses, $n_{shmDia1+3 + EHT\ 1864} = 153$ synapses.
1272 **(H)** Average number of ELVs per μm^2 in shCTR and shmDia1+3 boutons treated with 0.1 %
1273 DMSO (2.2 ± 0.2 for shCTR; 3.3 ± 0.3 for shmDia1+3, $p_{shCTR + DMSO \text{ vs } shmDia1+3 + DMSO} < 0.05$) or
1274 10 µM EHT 1864 (2.6 ± 0.3 for shCTR; 4.3 ± 0.4 for shmDia1+3, $p_{shCTR + DMSO \text{ vs } shmDia1+3 + EHT\ 1864}$

1275 < 0.001, $p_{shCTR + EHT\ 1864\ vs\ shmDia1+3 + EHT\ 1864} < 0.01$, Kruskal-Wallis test with Dunn's post-test) for

1276 2 h before fixation. Data represent mean ± SEM from $n_{shCTR + DMSO} = 144$ synapses, $n_{shmDia1+3 +}$

1277 $_{DMSO} = 143$ synapses, $n_{shCTR + EHT\ 1864} = 136$ synapses, $n_{shmDia1+3 + EHT\ 1864} = 153$ synapses.

1278

1279

1280

1281 **LEGENDS for SUPPLEMENTS**

1282 **List of supplemental figures**

1283 **Figure 1–figure supplement 1 | Role of formins and mDia1/3 in SV endocytosis.**

1284 **Figure 2–figure supplement 1 | SV depletion in mDia1/3-depleted neurons is activity**
1285 **dependent.**

1286 **Figure 3–figure supplement 1 | mDia1 binds membranes and localizes to presynaptic**
1287 **endocytic sites.**

1288 **Figure 4–figure supplement 1| mDia1 regulates presynaptic actin and SV endocytosis.**

1289 **Figure 5–figure supplement 1 | RhoA/B regulate SV endocytosis.**

1290 **Figure 6–figure supplement 1 | Cooperative action of mDia1/3 and Rac1 pathways in**
1291 **presynaptic endocytosis.**

1292 **Figure 7–figure supplement 1 | mDia1/3 and Rac1 cooperatively regulate the SV cycle and**
1293 **presynaptic ultrastructure.**

1294

1295 **Supporting Table 1 – Oligonucleotides used in this study**

1296 **Source Data Table**

1297 **Raw uncropped immunoblot images (merged PDF)**

Figure 1 S1

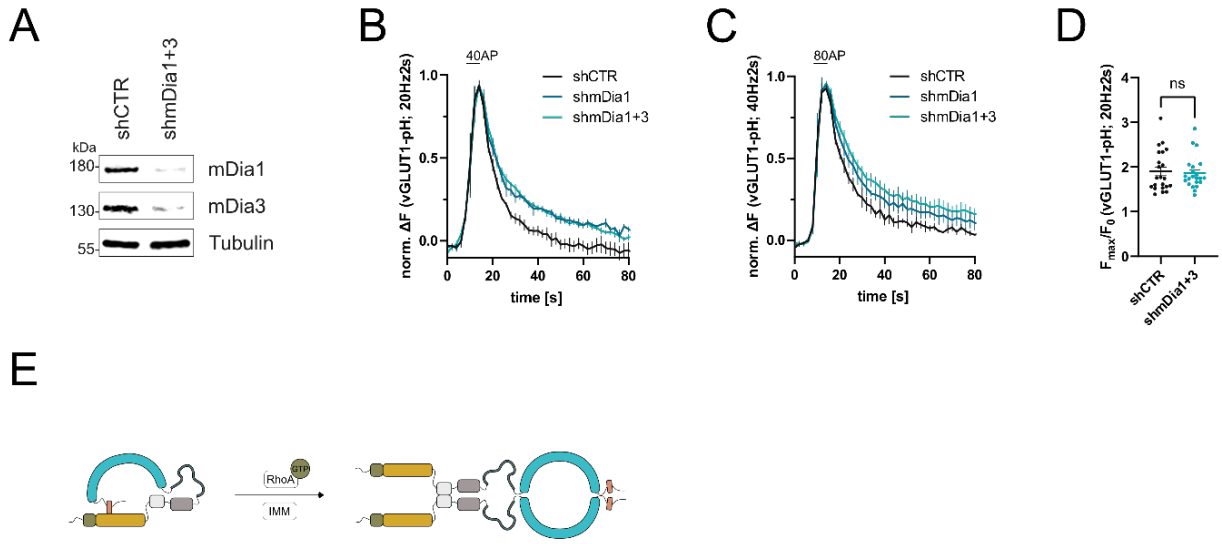

Figure 1 - Supplement 1 | Role of formins and mDia1/3 in SV endocytosis.

(A) Analysis of knockdown efficiency of lentiviral particles carrying shRNA against no mammalian target (shCTR) or mDia1 and mDia3 (shmDia1+3) in mouse hippocampal cultures harvested 12 days after transduction. Protein abundance of mDia1, mDia3 and Tubulin were immunoblotted with specific antibodies.

(B) Averaged normalized vGLUT1-pHluorin fluorescence traces from stimulated (40 APs; 20 Hz, 2 s) hippocampal neurons transduced with lentiviruses encoding shCTR, shmDia1 or both shmDia1 and shmDia3 combined (shmDia1+3). Data represent mean ± SEM. N = 4 independent experiments from n_{shCTR} = 17 videos, $n_{shmDia1}$ = 19 videos, $n_{shmDia1+3}$ = 18 videos. The corresponding endocytic decay constants are shown in figure 1G.

(C) Averaged normalized vGLUT1-pHluorin fluorescence traces for neurons transduced with shCTR, shmDia1 or shmDia1+3 in response to 80 AP stimulation (40 Hz, 2 s). Data represent mean ± SEM. N = 4 independent experiments from n_{shCTR} = 12 videos; $n_{shmDia1}$ = 15 videos; $n_{shmDia1+3}$ = 18 videos. Corresponding endocytic decay constants are shown in figure 1H.

1313 **(D)** Maxima of background-corrected vGLUT1-pHluorin fluorescence traces (surface normalized)
1314 for neurons transduced with shCTR (1.9 ± 0.1) or shmDia1+3 (1.9 ± 0.1) in response to 40 AP
1315 stimulation (20 Hz, 2 s). Data represent mean ± SEM. N = 22 independent experiments from n_{shCTR}
1316 = 105 videos and $n_{shmDia1+3}$ = 128 videos.
1317 **(E)** Schematic representation of the activation of mDia1. Binding of RhoA-GTP to the RBD
1318 domain (green) or application of mDia1 activator (IMM) competes with the intramolecular
1319 interaction of the N-terminal DID (yellow) with the C-terminal DAD (red) domain (see figure 3A
1320 for domain structure). The release of autoinhibition leads to dimerization of mDia formins in
1321 solution.
1322
1323

Figure 2 S1

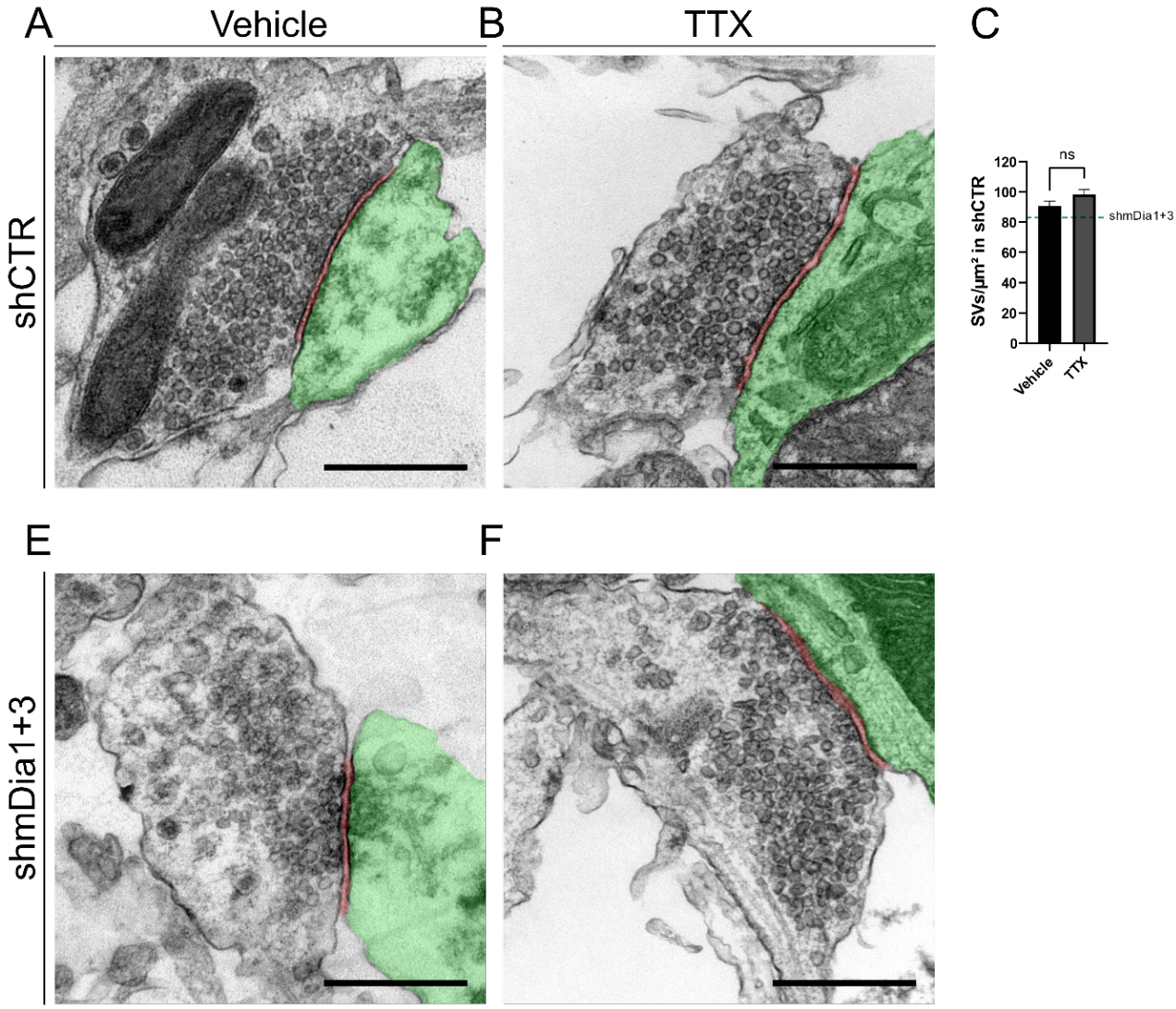

1324

1325 **Figure 2- Supplement 1 | SV depletion in mDia1/3-depleted neurons is activity dependent.**

1326 **(A,B)** Representative synaptic electron micrographs from neurons transduced with shCTR and

1327 treated with 0.1% Vehicle (A) or 1 µM TTX (B) for 36 h before fixation. Postsynapse and

1328 postsynaptic cleft are colored in green and maroon, respectively. Scale bar, 250 nm.

1329 **(C)** Average number of SV per μm^2 in synaptic boutons of neurons transduced with shCTR and

1330 treated with 0.1 % Vehicle (A; 90.7 ± 3.1) or 1 µM TTX (B; 98.4 ± 3.3) for 36 h before chemical

1331 fixation. Data shown represent the mean ± SEM from two independent experiments and $n_{Vehicle}$ =

1332 180, n_{TTX} = 204 synapses. The dotted line represents the average SV numbers/μm^2 in shmDia1+3
1333 boutons treated with DMSO from the same experiments as a reference.
1334 **(D,E)** Representative synaptic electron micrographs from neurons transduced with shmDia1+3
1335 and treated with 0.1% Vehicle (D) or 1 μM TTX (E) for 36 h before fixation. Postsynapse and
1336 postsynaptic cleft are colored in green and maroon, respectively. Scale bar, 250nm. Average
1337 number of SV per μm^2 in boutons is shown in figure 2D.
1338

Figure 3 S1

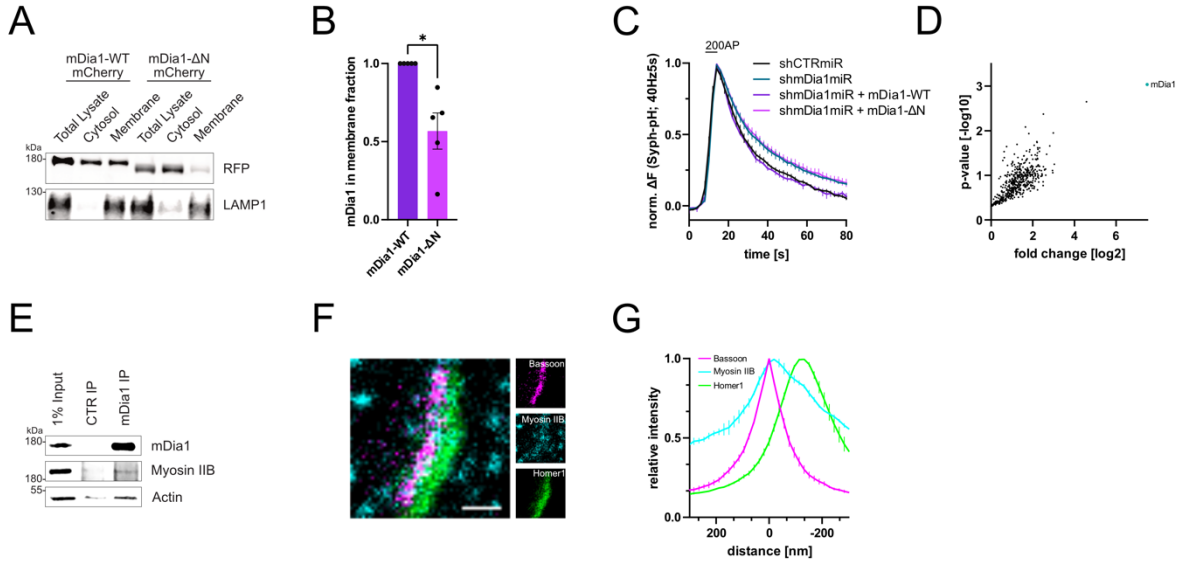

Figure 3 - Supplement 1 | mDia1 binds membranes and localizes to presynaptic endocytic sites.

(A) Membrane levels of mDia1-WT-mCherry versus mDia1-ΔN-mCherry proteins overexpressed in HEK293T cells. Membrane and cytosolic cellular fractions were isolated by ultracentrifugation and analyzed by immunoblotting with specific antibodies (LAMP1) and in-gel fluorescence of mCherry tags.

(B) Densitometric quantification of mDia1-WT versus mDia1-ΔN (0.6 ± 0.1; $p < 0.05$, one sample t-test) membrane-associated protein levels. Data shown are normalized to mDia1-WT (set to 1) and expressed as mean ± SEM. Representative immunoblot is shown in A. N = 5 independent experiments.

(C) Averaged normalized Synaptophysin-pHluorin fluorescence from stimulated (200 APs, 40 Hz, 5s) hippocampal neurons transfected with shCTRmiR or shmDia1miR. For rescue experiments, neurons were co-transfected with plasmids encoding mDia1-WT-mCherry, mDia1-ΔN-mCherry or mCherry alone (shCTRmiR & shmDia1miR). Endocytic decay constants are shown in figure 3B.

1355 **(D)** Full volcano plot of proteins from figure 3E associating with synaptic mDia1 analyzed by
1356 label-free proteomics of anti-mDia1 versus CTR immunoprecipitates from detergent-extracted
1357 mouse synaptosomes (P2' fraction). The cyan dot shows the specific enrichment of mDia1 as the
1358 bait protein of the immunoprecipitation ($p < 0.001$, two-tailed student's t-test). N = 3 independent
1359 experiments.
1360 **(E)** Endogenous co-immunoprecipitation of Myosin IIB by mDia1 from detergent-extracted
1361 mouse synaptosomes (P2' fraction). Samples were analyzed by immunoblotting using specific
1362 antibodies against mDia1, Myosin IIB and β-Actin.
1363 **(F)** Representative three-channel time-gated STED image of a synapse from hippocampal cultures
1364 fixed and immunostained for Bassoon (presynaptic marker, magenta), Myosin IIB (cyan) and
1365 Homer1 (postsynaptic marker, green). Scale bar, 250 nm.
1366 **(G)** Averaged normalized line profiles for synaptic distribution of Myosin IIB and Homer1 relative
1367 to Bassoon (Maximum set to 0 nm). Data are expressed as mean ± SEM. N = 3 independent
1368 experiments from n = 267 synapses.
1369

Figure 4 S1

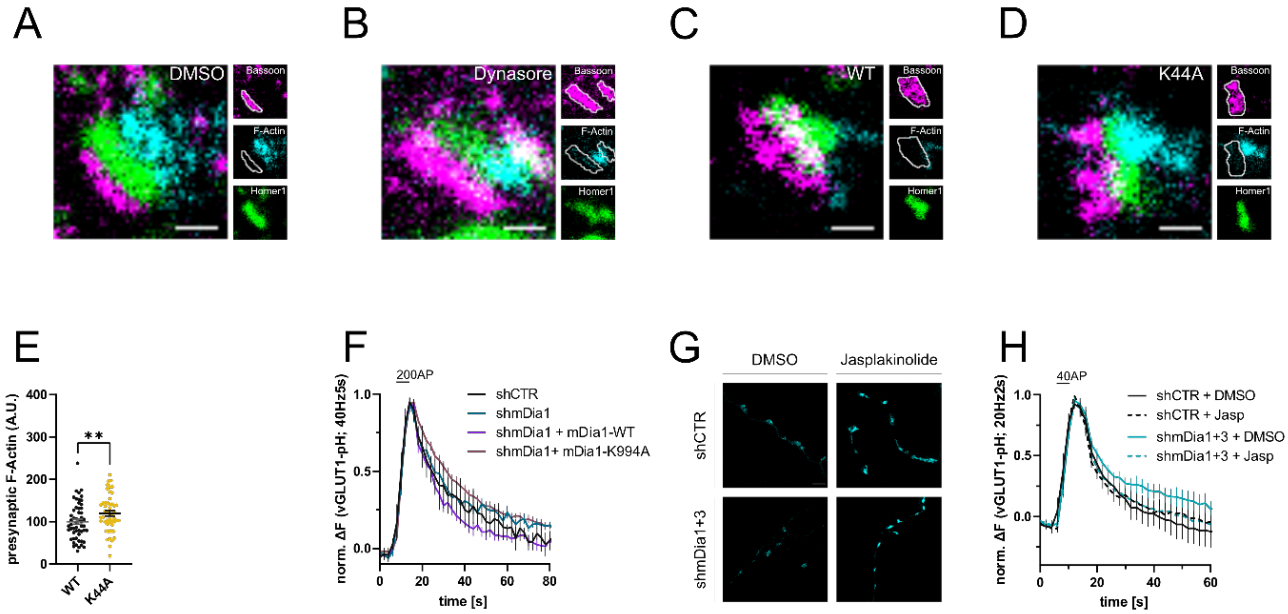

Figure 4 - Supplement 1 | mDia1 regulates presynaptic actin and SV endocytosis.

(A,B) Representative three-channel time-gated STED images of synapses from hippocampal cultures treated with 0.1% DMSO (A) or 80 µM Dynasore (B) for 10 min. Cells were fixed and stained for Bassoon (magenta), F-Actin (cyan) and Homer1 (green). Synapses from A and B stem from the same experiment and brightness and contrast of all three channels were set to the same values. Scale bar, 250 nm. Corresponding analysis of presynaptic F-Actin levels is shown in figure 4C.

(C,D) Representative three-channel time-gated STED images of synapses from hippocampal cultures transduced with Dynamin1-WT (C) or Dynamin1-K44A (D). Cells were fixed and stained for Bassoon (magenta), F-Actin (cyan) and Homer1 (green). Synapses from C and D stem from the same experiment and brightness and contrast of all three channels were set to the same values. Scale bar, 250 nm.

1384 **(E)** Presynaptic F-Actin levels in synapses from neurons transduced with Dynamin1-WT (C; 100
1385 ± 5.9) or Dynamin1-K44A (D; 119.8 ± 6.2, $p < 0.01$, one sample t-test). Absolute line profiles of
1386 F-Actin overlapping with Bassoon (presynapse) distribution were integrated. Data shown are
1387 normalized to WT (set to 100) and expressed as mean ± SEM. n_{WT} = 54 synapses, n_{K44A} = 49
1388 synapses.
1389 **(F)** Averaged normalized vGLUT1-pHluorin fluorescence traces for neurons transduced with
1390 shCTR or shmDia1 in response to 200 AP (40 Hz, 5s) stimulation. For rescue purposes, cells were
1391 co-transduced with mDia1-WT-SNAP or mDia1-K994A-SNAP. Data are expressed as mean ±
1392 SEM. N = 6 independent experiments from n_{shCTR} = 21 videos; $n_{shmDia1}$ = 21 videos; $n_{shmDia1 + mDia1-}$
1393 $_{WT}$ = 16 videos; $n_{shmDia1 + mDia1-K994A}$ = 19 videos. Corresponding endocytic decay constants are
1394 shown in figure 4D.
1395 **(G)** Representative STED images of endogenous β-Actin in vGLUT1 positive synapses in
1396 hippocampal neurons transduced with shCTR or shmDia1+3 and treated with 0.1 % DMSO or
1397 1 µM Jasplakinolide for 45 min. Neurons were co-transfected with pOrange-GFP-β-Actin knockin
1398 and vGLUT1-mCherry plasmids before fixation and immunostaining. Scale bar, 2.5 µm.
1399 **(H)** Averaged normalized vGLUT1-pHluorin fluorescence traces for neurons transduced with
1400 shCTR or shmDia1+3 in response to 40 AP (20 Hz, 2s) stimulation. Neurons were pre-incubated
1401 with 0.1 % DMSO or 1 µM Jasplakinolide (Jasp) for 30 min in the cell media before imaging.
1402 Data are expressed as mean ± SEM. N = 6 independent experiments from $n_{shCTR + DMSO}$ = 32 videos,
1403 $n_{shmDia1+3 + DMSO}$ = 35 videos, $n_{shCTR + Jasp}$ = 33 videos; $n_{shmDia1+3 + Jasp}$ = 34 videos. The corresponding
1404 endocytic decay constants are shown in figure 4I.
1405

Figure 5 S1

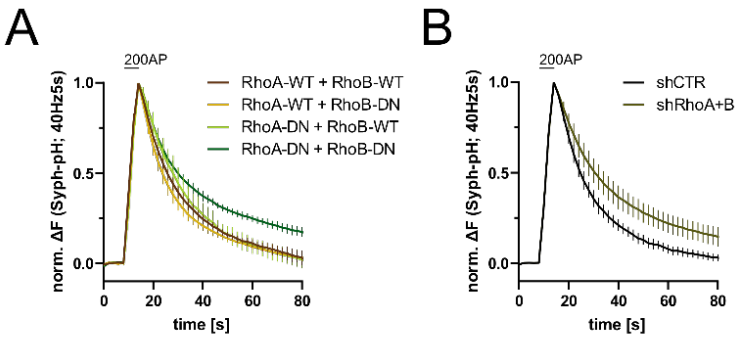

Figure 5 - Supplement 1 | RhoA/B regulate SV endocytosis.

(A) Averaged normalized Synaptophysin-pHluorin fluorescence traces from stimulated (200 APs; 40 Hz, 5s) hippocampal neurons transfected with plasmids encoding the indicated combinations of WT or DN RhoA and RhoB variants. Data represent mean ± SEM. N = 3 independent experiments from $n_{RhoA\text{-}WT + RhoB\text{-}WT}$ = 21 videos, $n_{RhoA\text{-}DN + RhoB\text{-}WT}$ = 31 videos, $n_{RhoA\text{-}WT + RhoB\text{-}DN}$ = 23 videos, $n_{RhoA\text{-}DN + RhoB\text{-}DN}$ = 22 videos. Endocytic decay constants are shown in figure 5D.

(B) Averaged normalized Synaptophysin-pHluorin fluorescence traces from stimulated (200 APs; 40 Hz, 5s) hippocampal neurons transfected with shRNA against no mammalian target (shCTR) or against RhoA and RhoB (shRhoA+B). Data represent mean ± SEM. N = 3 independent experiments from n_{shCTR} = 27 videos, $n_{shRhoA+B}$ = 25 videos.

Figure 6 S1

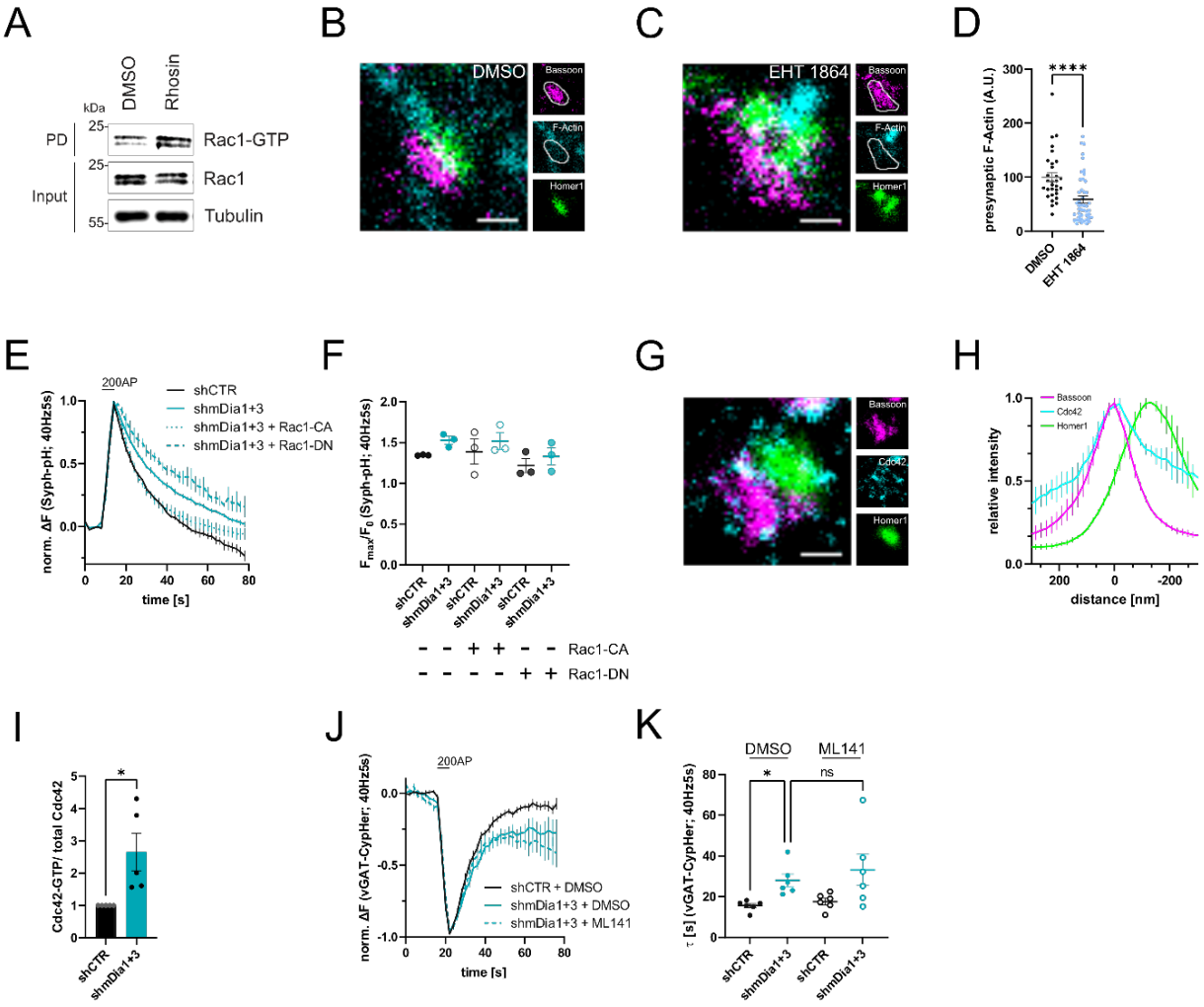

Figure 6 - Supplement 1 | Cooperative action of mDia1/3 and Rac1 pathways in presynaptic endocytosis.

(A) Analysis of Rac1 activity by Rac1-GTP pulldown (PD) from whole-cell lysates (input) of mouse hippocampal cultures upon inhibition of Rho activity utilizing immobilized PAK as bait. Cells were treated with 0.1 % DMSO or 10 µM Rho Inhibitor (Rhosin) for 2 h before harvest. Samples were analyzed by immunoblotting for Rac1 and Tubulin using specific antibodies. Input, 10% of material used for the pulldown. Contrast of pulldown and input blots was seperatly adjusted for visualisation purposes.

1427 **(B,C)** Representative three-channel time-gated STED images of synapses from hippocampal
1428 cultures treated with 0.1 % DMSO or 10 µM Rac1 Inhibitor (EHT 1864) for 2 h. Cells were fixed
1429 and stained for Bassoon (magenta), F-Actin (cyan) and Homer1 (green). Scale bar, 250 nm.
1430 **(D)** Presynaptic F-Actin levels in synapses of neurons treated with 0.1 % DMSO (100 ± 8.5) or
1431 10 µM Rac1 Inhibitor (EHT 1864; 58.6 ± 6.5; $p < 0.0001$, one sample Wilcoxon test) for 2 h. Line
1432 profiles of F-Actin overlapping with Bassoon (presynapse) distribution were integrated. Data
1433 shown are normalized to DMSO (set to 100) and expressed as mean ± SEM. $n_{DMSO} = 30$, $n_{EHT\ 1864}$
1434 = 46 from two independent experiments.
1435 **(E)** Averaged normalized Synaptophysin-pHluorin fluorescence traces from stimulated (200 APs;
1436 40 Hz, 5s) hippocampal neurons transduced with lentiviruses encoding shCTR or shmDia1+3 and
1437 transfected with plasmids for expression of constitutively-active Rac1 (Rac1-CA; Q61L variant)
1438 or dominant-negative Rac1 (Rac1-DN; T17N variant). Data represent mean ± SEM. N = 3
1439 independent experiments from $n_{shCTR} = 12$ videos, $n_{shmDia1+3} = 23$ videos, $n_{shCTR\ +\ Rac1\text{-}CA} = 10$
1440 videos, $n_{shmDia1+3\ +\ Rac1\text{-}CA} = 14$ videos, $n_{shCTR\ +\ Rac1\text{-}DN} = 9$ videos; $n_{shmDia1+3\ +\ Rac1\text{-}DN} = 13$ videos.
1441 The corresponding endocytic decay constants are shown in figure 6H.
1442 **(F)** Maxima of background-corrected Synaptophysin-pHluorin fluorescence traces (surface
1443 normalized maximum values of traces shown in E) from stimulated (200 APs; 40 Hz, 5s)
1444 hippocampal neurons transduced with lentiviruses encoding shCTR ($F_{max}/F_0 = 1.3 \pm 0.0$) or
1445 shmDia1+3 ($F_{max}/F_0 = 1.5 \pm 0.0$) and transfected with plasmics encoding CA ($F_{max}/F_{0\ shCTR\ +\ Rac1\text{-}}$
1446 $_{CA} = 1.4 \pm 0.2$; $F_{max}/F_{0\ shmDia1+3\ +\ Rac1\text{-}CA} = 1.5 \pm 0.1$) or DN versions (($F_{max}/F_{0\ shCTR\ +\ Rac1\text{-}DN} = 1.2 \pm$
1447 0.1; $F_{max}/F_{0\ shmDia1+3\ +\ Rac1\text{-}DN} = 1.3 \pm 0.1$) of Rac1. Data represent mean ± SEM.
1448 **(G)** Representative three-channel time-gated STED image of a synapses from hippocampal mouse
1449 cultures, fixed and immunostained for Bassoon (magenta), Cdc42 (cyan) and Homer1 (green).
1450 Scale bar, 250 nm.

1451 **(H)** Averaged normalized line profiles for synaptic distribution of Cdc42 and Homer1 relative to
1452 Bassoon (Maximum set to 0 nm). Data are expressed as mean ± SEM (N = 3; n = 96 synapses).
1453 **(I)** Densitometric quantification of Cdc42-GTP normalized to total Cdc42 levels in lysates from
1454 shmDia1+3 neurons (2.7 ± 0.6; $p < 0.05$, one sample t-test).Values for shCTR were set to 1. Data
1455 are expressed as mean ± SEM from N = 3 independent experiments.
1456 **(J)** Averaged normalized vGAT-CypHer fluorescence traces for neurons transduced with shCTR
1457 or shmDia1+3 in response to 200 AP (40 Hz, 5s) stimulation. Cells were acutely treated with 0.1
1458 % DMSO or 10 µM Cdc42 Inhibitor (ML141) in the imaging buffer. Data shown represent the
1459 mean ± SEM. N = 6 independent experiments from $n_{shCTR + DMSO}$ = 31 videos, $n_{shmDia1+3 + DMSO}$ =
1460 33 videos, $n_{shmDia1+3 + ML141}$ = 32 videos.
1461 **(K)** Endocytic decay constants of vGAT-CypHer traces in I: $\tau_{shCTR + DMSO}$ = 15.6 ± 1.0 s, $\tau_{shmDia1+3}$
1462 $_{+ DMSO}$ = 28.0 ± 3.1 s, $\tau_{shCTR + ML141}$ = 17.6 ± 1.6 s, $\tau_{shmDia1+3 + ML141}$ = 33.1 ± 7.7 s; $p_{shCTR + DMSO \text{ vs}}$
1463 $_{shmDia1+3 + DMSO} < 0.01$, Kruskal-Wallis test with Dunn's post-test. Data shown represent the mean
1464 ± SEM. N = 6 independent experiments from $n_{shCTR + DMSO}$ = 31 videos, $n_{shmDia1+3 + DMSO}$ = 33
1465 videos, $n_{shCTR + ML141}$ = 29 videos, $n_{shmDia1+3 + ML141}$ = 32 videos.
1466

Figure 7 S1

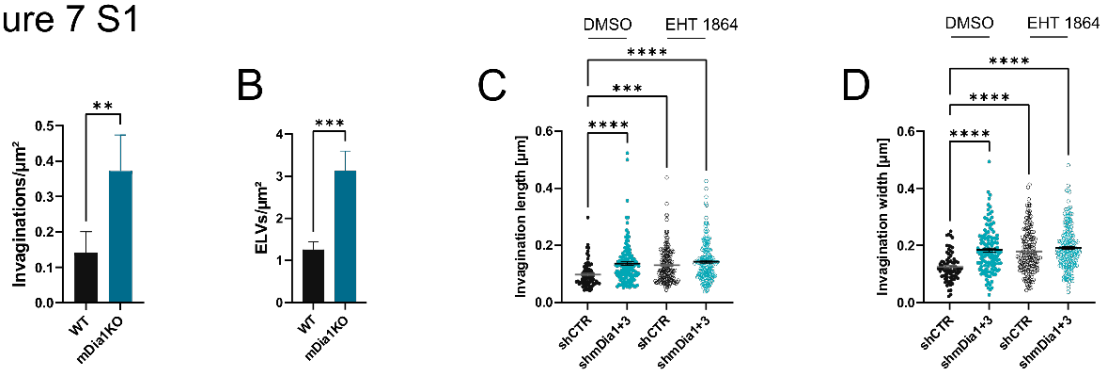

Figure 7- Supplement 1 | mDia1/3 and Rac1 cooperatively regulate the SV cycle and presynaptic ultrastructure.

(A) Average number of invaginations per µm^2 in WT (0.1 ± 0.1) and mDia1 KO (0.4 ± 0.1; $p < 0.01$, Mann-Whitney test) boutons. Data shown represent the mean ± SEM from $n_{WT} = 103$ synapses, $n_{KO} = 96$ synapses.

(B) Average number of ELVs per µm^2 in WT (1.3 ± 0.2) and mDia1KO (3.1 ± 0.5; $p < 0.001$, Mann-Whitney test) boutons. Data shown represent the mean ± SEM from $n_{WT} = 103$ synapses, $n_{KO} = 96$ synapses.

(C) Average invagination length in shCTR and shmDia1+3 boutons treated with 0.1 % DMSO (97.6 ± 4.5 nm for shCTR; 136.8 ± 6.0 nm for shmDia1+3, $p_{shCTR + DMSO \text{ vs } shmDia1+3 + DMSO} < 0.0001$) or 10 µM EHT 1864 (130.9 ± 4.5 nm for shCTR, $p_{shCTR + DMSO \text{ vs } shCTR + EHT\ 1864} < 0.001$; 143.1 ± 4.9 nm for shmDia1+3, $p_{shCTR + DMSO \text{ vs } shmDia1+3 + EHT\ 1864} < 0.0001$, Kruskal-Wallis test with Dunn's post-test) for 2 h before chemical fixation. Data represent mean ± SEM from $n_{shCTR + DMSO} = 77$ invaginations, $n_{shmDia1+3 + DMSO} = 141$ invaginations, $n_{shCTR + EHT\ 1864} = 176$ invaginations, $n_{shmDia1+3 + EHT\ 1864} = 189$ invaginations.

1484 **(D)** Average invagination width in shCTR and shmDia1+3 boutons treated with 0.1 % DMSO
1485 (124.5 ± 5.6 nm for shCTR; 184.1 ± 6.6 nm for shmDia1+3, $p_{shCTR + DMSO \text{ vs } shmDia1+3 + DMSO} <$
1486 0.0001) or 10 µM EHT 1864 (179.0 ± 5.8 nm for shCTR, $p_{shCTR + DMSO \text{ vs } shCTR + EHT\ 1864} < 0.0001$;
1487 191.0 ± 5.4 nm for shmDia1+3, $p_{shCTR + DMSO \text{ vs } shmDia1+3 + EHT\ 1864} < 0.0001$, Kruskal-Wallis test with
1488 Dunn's post-test) for 2 h before chemical fixation. Data represent mean ± SEM from $n_{shCTR + DMSO}$
1489 = 77 invaginations, $n_{shmDia1+3 + DMSO}$ = 141 invaginations, $n_{shCTR + EHT\ 1864}$ = 176 invaginations,
1490 $n_{shmDia1+3 + EHT\ 1864}$ = 189 invaginations.
1491
1492